TECHNISCHE
UNIVERSITÄT
WIEN

Cherenkov diffraction radiation in beam diagnostics

investigation of a potential tool for FCC-ee

MASTER'S THESIS

submitted in partial fulfillment of the requirements for the degree of

Master of Science

in

Technical Physics

by

Andreas Schlögelhofer
Registration Number 01426875

conducted at the Institute of Atomic and Subatomic Physics
at the Faculty of Physics at TU Wien

in cooperation with the
European Organization for Nuclear Research

under the supervision of
Thibaut Lefèvre and **Michael Benedikt**

Geneva, December 2020

Abstract

In recent years the investigation of Cherenkov diffraction radiation produced by charged particles passing in close vicinity of dielectric material led to promising prototypes for beam diagnostics [JMS$^+$19, Lef19b, BAK$^+$19]. In this report, we present a simulation approach to investigate the radiated energy spectrum from Cherenkov diffraction radiation of a single particle and a particle bunch with a focus on its exploitation for the Future Circular Collider for electrons and positrons (FCC-ee).

The radiated energy spectra of a single particle from two analytical models that describe a flat and a cylindrical radiator geometry respectively are discussed. Different radiation regimes are characterized within the various spectra and their dependency on key beam parameters is evaluated. Proceeding with the radiated energy spectrum of a bunch of particles, the formation of a coherent and an incoherent radiation regime is demonstrated.

As both regimes have their distinct characteristics, the analysis is split into two parts for the radiated energy spectra of the different bunch profiles at FCC-ee. For incoherent photons emitted in the visible spectrum, the application of a beam position monitor, as well as the bunch-by-bunch measurement of the longitudinal bunch profile over several turns are investigated. For coherent radiation emitted in the multi GHz range, the application of a beam position monitor operating with bandpass filters and a bunch length measurement relying on power measurements at different frequencies are discussed.

All these applications could profit from the unique characteristics of Cherenkov diffraction radiation. Its high directivity would allow to minimize background contribution and as it is a non-invasive technique it has minimal impact on the accelerated particles, which makes it a perfect candidate for future beam instrumentation devices.

Contents

1

Future Circular Collider for electrons and positrons (FCC-ee)

1.1 Introduction FCC-ee

The Future Circular Collider for electrons and positrons (FCC-ee) is a proposed electron-positron collider expanding the existing accelerator infrastructure at the European Organization for Nuclear Research (CERN) in Meyrin, Geneva, Switzerland. A detailed report on the conceptual design of this novel lepton collider was published in 2019 [AAA+19]. Following this report a short introduction is given here to provide the key data of the project.

Currently four e^+e^- collider designs are being investigated around the world aiming to study the properties of the matter in our universe. Besides FCC-ee, namely the International Linear Collider (ILC) in Japan, the Compact Linear Collider (CLIC) in Switzerland and the Circular Electron Positron Collider (CEPC) in China. From all four of them FCC-ee proposes to achieve the highest luminosities throughout its energy range. It will be a precision instrument for investigating the properties of the Z and W bosons, the Higgs boson and the top (anti)quark with an unprecedented amount of production samples. The expected sample numbers during the whole operation of FCC-ee accumulate to 5×10^{12} (Z), 10^8 (W^+W^-) and 10^6 (Higgs and $t\bar{t}$ respectively) for the different operation modes. As these four fundamental particle types are the ones with the greatest mass as can be seen in Fig. 1.1 high energies are required for their production. E.g. for the $t\bar{t}$ production a collision energy of about 365 GeV is required.

The general layout of the machine is a double-ring configuration with common

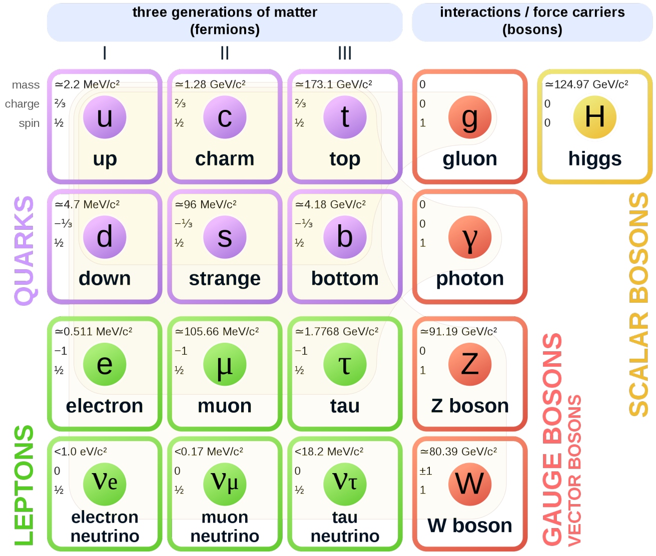

Figure 1.1: The standard model of particle physics [Cus20]. The heaviest particles (Z and W boson, Higgs boson and top quark) also denote the different operation modes of FCC-ee in this report.

beam pipe sections close to the interaction points. The proposed tunnel has a circumference of 97.756 km. The same tunnel would be used to host a hadron collider after the FCC-ee lifetime. In order to house all the necessary equipment and provide enough space for transport the inner diameter of the tunnel is 5.5 m. Besides the main tunnel roughly 8 km of bypass tunnels, 18 shafts, 14 large caverns and 12 new surface sites are foreseen.

As shown in Fig. 1.2 the baseline is not a perfect circle but rather a slightly deformed one to create straight sections where the production of synchrotron radiation is reduced. In these straight sections the interaction points and the radiofrequency systems will be located. The implementation from two up to four interaction points is discussed at the moment.

In Tab. 1.1 the machine parameters for all the four operation modes are provided. Typically the equilibrium beam parameters in electron storage rings are defined by synchrotron radiation which is produced when the direction of propagation of charged particles is changed to keep them on a circular path. For FCC-ee also beamstrahlung has a significant impact on energy spread and lifetime of the beam. Beamstrahlung can be considered as a special type of radiation where a bunch emits photons as it is decelerated due to the presence of the electromagnetic field of the counter propagating bunch.

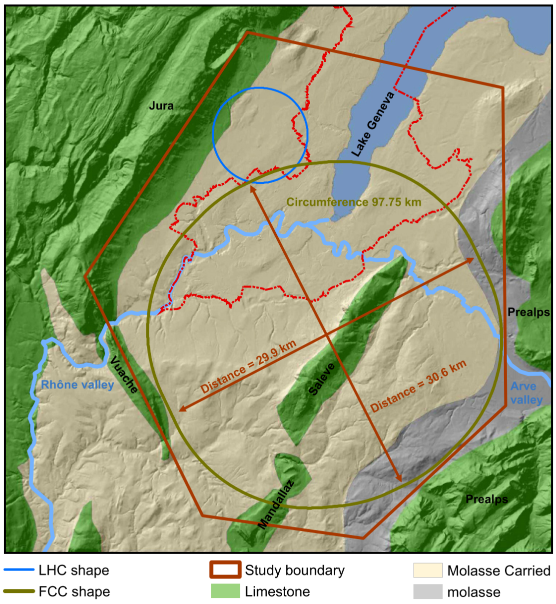

Figure 1.2: Illustration of the FCC tunnel baseline featuring the main topological and geological conditions in its surroundings. The LHC tunnel (circumference of 26.659 km) is shown in dark blue [AAA+19, p. 441].

		Z	**WW**	**H(ZH)**	**$t\bar{t}$**
Circumference	[km]	97.756			
Bending radius	[km]	10.760			
Sync. radiation power per beam	[MW]	50			
Beam energy	[GeV]	45	80	120	182.5
Beam current	[mA]	1390	147	29	5.4
Number of bunches/beam		16640	2000	393	48
Bunch intensity	[10^{11}]	1.7	1.5	1.5	2.3
Hor. geometric emittance	[nm]	0.27	0.28	0.63	1.46
Ver. geometric emittance	[pm]	1.0	1.7	1.3	2.9
Bunch length with sync. radiation	[mm]	3.5	3.0	3.2	2.0
Bunch length with beamstrahlung	[mm]	12.1	6.0	5.3	2.5

Table 1.1: Characteristics of FCC-ee [AAA+19, p. 283].

1.2 FCC-ee beam instrumentation specific needs

This section presents the requirements to be met and the difficulties to be overcome regarding the beam instrumentation for FCC-ee. It is based on a section dedicated to beam diagnostics in the FCC-ee conceptual design report [AAA$^+$19, Chapter 3.6] as well as on a talk from FCC Week 2019 in Brussels by T. Lefèvre [Lef19a].

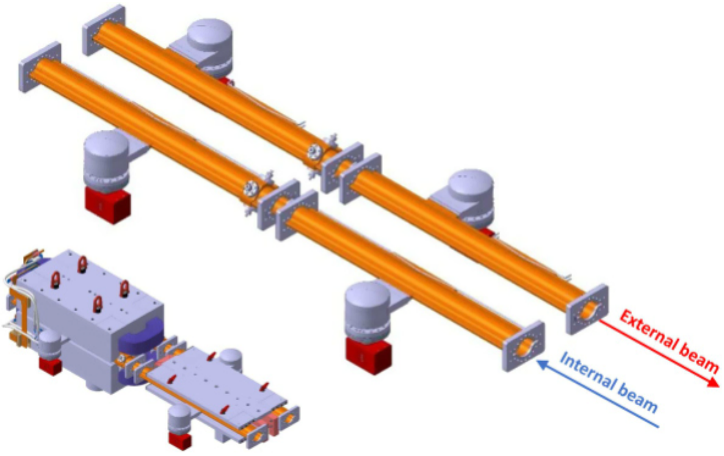

Figure 1.3: Schematic of the FCC-ee vacuum system. A fraction of the two main rings in the arcs is shown [AAA$^+$19, p. 403].

As a starting point for the beam instrumentation requirements for FCC-ee we need to have a look at the design beam parameter values given in Tab. 1.1. From this list, it is important to understand what dynamic range all beam instruments will have to cover. Moreover, we focus on those parameters most relevant for the possible application of Cherenkov diffraction radiation. An overview of these parameters and their ranges is provided in Tab. 1.2. It can be seen that the bunch intensity is in the same order of magnitude for the four different operation modes, however, the filling scheme varies significantly for the different beam energies. The number of bunches per beam ranges from 48 for operation at top energy and 16640 for operation at the Z pole. Thus beam current is reduced from 1390 mA to 5.4 mA in order to cope with the increasing high flux of synchrotron radiation emitted at high energy. This was done by design to limit the synchrotron power to an acceptable limit for all beam energies. The high beam intensity and wakefield effects would induce significant heat load on the beam instrumentation devices, synchrotron radiation would lead to a high radiation dose especially in the arcs. Therefore active cooling and shielding of the instruments may be needed. The front end electronics will require a radiation hard design. On top of that close to the interaction points in the high luminosity regions the radiation level would be significantly elevated.

		Min.	Max.
Number of bunches/beam		48	16640
Bunch intensity	[10^{11}]	1.5	2.3
Beam current	[mA]	5.4	1390
Bunch spacing	[ns]	2.5	4000
Bunch length	[ps]	6	40
Transverse size in arcs (hor.)	[μm]	60	150
Transverse size in arcs (ver.)	[μm]	10	20

Table 1.2: FCC-ee beam parameters relevant for beam diagnostic devices [AAA+19, p. 424].

1.2.1 Beam position monitor (BPM)

To focus the particle beams FCC-ee will use 1450 main quadrupoles per ring. Every quadrupole requires a separate BPM and in addition to that for long straight regions and close to the interaction regions additional BPMs are needed. This results in 2000 BPMs per ring, so 4000 BPMs in total. Another 2000 BPMs are foreseen in the booster rings. As seen in Fig. 1.4 the electrodes in the main rings will be mounted at 45° with respect to the horizontal plane to reduce the impact of synchrotron radiation.

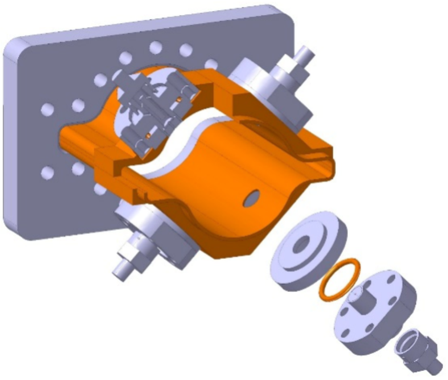

Figure 1.4: Schematic of the FCC-ee vacuum pipe with four button electrodes [KG19].

In Tab. 1.1 the targeted geometric emittances are shown, which range from 0.27 − 1.46 nm in the horizontal and from 1.0−2.9 pm in the vertical. This extremely small targeted emittances require an alignment of the machine with a precision of at least 50 μm. Orbit measurements require a sub-micron resolution. To monitor injection oscillations and for optics measurements turn-by-turn data must be provided. Even though the nominal diameter of the FCC-ee vacuum pipe shown in Fig. 1.4 is 70 mm the use of special BPMs in the long straight sections of the accelerator may allow different beam pipe dimensions.

1.2.2 Transverse bunch size

Bunch size measurements in the transverse plane are needed on a bunch-by-bunch basis. This data is then processed to determine the beam emittance. Typically X-ray imaging of synchrotron radiation [MTTS15] and visible light interferometry [CHL$^+$17] are used to measure such small beam sizes, but in FCC-ee they are limited by diffraction effects due to the high beam energies. Possible alternatives are under investigation and include X-ray interferometers using a two-slit setup [MOZ16] or near-field speckles [SPP$^+$17].

1.2.3 Longitudinal bunch size

Just as for the transverse bunch size also the bunch length must be monitored bunch-by-bunch. To determine the effect of beamstrahlung at the interaction points the bunch lengths have to be provided for every turn. For theses turn-by-turn measurements a resolution of 1 ps is required. A precise measurement of the energy spread is necessary for energy calibration and requires bunch length measurements with even higher resolution. However, this sub-picosecond resolution of the bunch profiles can be obtained within a few minutes of measurement time and therefore accumulated over many turns. To measure bunches of several picosecond in length with a sub-picosecond resolution beam instrumentation devices with a high dynamic range have to be realized.

1.3 Considering Cherenkov diffraction radiation (ChDR) for FCC-ee

Past experiments on Cherenkov diffraction radiation have shown its promising capabilities for beam diagnostic techniques. It might enable us to design non-invasive diagnostics which benefit from the high directivity and the large angles of ChDR emission [L+18]. The exploitation of incoherent radiation produced by high energy particles of several GeV has been shown at Cornell Electron Storage Ring (CESR) in Ithaca, New York, United States. Applications with coherent radiation at lower particle energies of about 200 MeV have been demonstrated at CERN Linear Electron Accelerator for Research (CLEAR) in Meyrin, Geneva, Switzerland.

Incoherent ChDR at CESR

The experiments performed by Kieffer et al. at CESR led to the direct observation of incoherent ChDR in the visible spectrum [KBB+18]. For the performed experiments flat and prismatic radiators made out of fused silica (SiO_2, $\epsilon_r[0.2 - 2\mu\text{m}] \approx 2.1$) have been used. A few example images which were used to calculate the photon emission and to measure the horizontal beam profile are shown in Fig. 1.5. These images show different distances between the beam and the surface of the radiator, referred to as impact parameters.

Particle types	e^- and e^+
Beam energy [GeV]	2.1 / 5.3
Bunch intensity	1.6×10^{10}
Ring circumference [m]	768.4

Table 1.3: Beam parameters at CESR [KBB+18].

The photon emission was measured for a range of impact parameters and an exponential increase of the photon emission when reducing the impact parameter was demonstrated. This was also in good agreement with data from simulations based on [SK14, Eq. 18] which describes the angular distribution of polarization radiation. The decay of the radiated energy at high frequencies is explained by introducing the effective radius r_{eff} of the particles electromagnetic field [Cas97]. It is given as

$$r_{eff} = \frac{\gamma\lambda}{2\pi}, \tag{1.1}$$

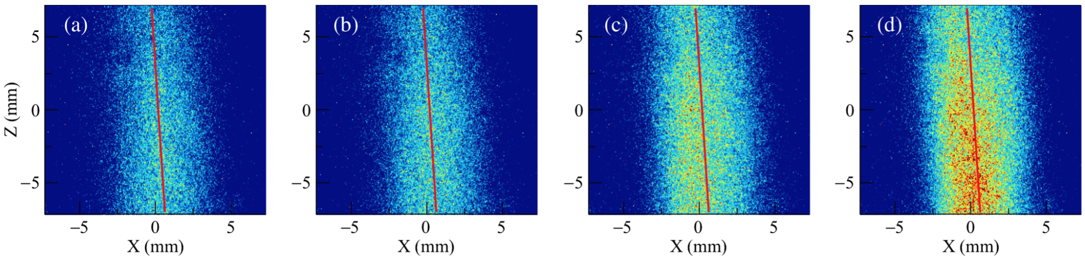

Figure 1.5: Images of the radiator surface for different impact parameters (a) 1.37, (b) 1.32, (c) 1.08, (d) 0.9 mm. The red line indicates the beam trajectory underneath the radiator. [KBB$^+$18]

where λ is the radiation wavelength and $\gamma = 1/\sqrt{1-(v/c)^2}$ the Lorentz factor. For shorter wavelengths the light yield drops significantly due to the decrease of the effective radius. For longer wavelengths with an effective radius which exceeds the impact parameter the photon yield decreases $\propto 1/\lambda^3$ as it does for Cherenkov radiation characterized by Frank and Tamm [FT37].

Coherent ChDR at CLEAR

The experimental studies performed by Curcio et al. [CBC$^+$20] have demonstrated the non-invasive bunch length measurement of ps-bunches using ChDR at the CLEAR test facility [G$^+$18]. They also showed the possibility of measuring the beam position using the same setup. For the study a dielectric prism made out of PTFE ($\epsilon_r = 2.1$) was used. To measure the produced ChDR three detectors each consisting of a waveguide horn, a band pass filter and a Schottky diode were installed. They measured the radiation at 60 ± 1 GHz, 84 ± 1 GHz and 113.5 ± 9 GHz respectively and were pointing at one surface of the prism each.

Particle type	e^-
Beam energy [MeV]	60 - 220
Bunch intensity	$6.2 \times 10^7 - 3.1 \times 10^9$
Bunch length [ps]	0.5 - 10

Table 1.4: Beam parameters at CLEAR [SAL$^+$19, CBC$^+$20].

In Fig. 1.6a the measurement of the beam position used to center the bunch in the radiator to set up the system before performing the bunch length measurement is shown. Besides the beam position measurements, in Fig. 1.6a also simulations performed with VSim are shown, which clearly indicate the same trend.

To perform the bunch length measurements the coherent spectrum has been measured at different frequencies. From that a Gaussian bunch can be reconstructed and its bunch length determined. The bunch length measurement relies on the measured power at the two different frequencies. Moreover, the impact parameter as well as the particle energy has to be known. The final results from these measurements are presented in Fig. 1.6b together with simulations from VSim and compared to measurements performed with a radio frequency deflector. They agree especially for short bunches up to 2 ps. The larger error for longer bunch lengths is due to the fact that the coherent spectrum of longer bunches gets weaker at higher measurement frequencies.

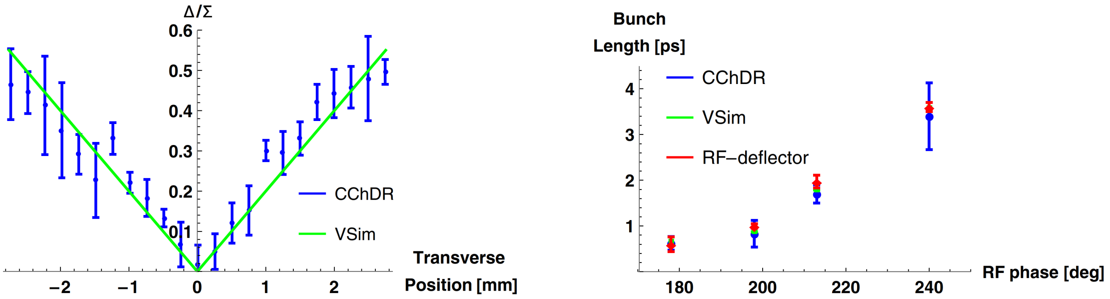

(a) Transverse beam position measurement in the horizontal plane.

(b) Bunch length measurements of Gaussian bunches.

Figure 1.6: Bunch position and length measurement at CLEAR [CBC+20].

1.3.1 Conclusions for FCC-ee from past experiments

The experiments performed at CESR have shown that the incoherent spectrum of ChDR can be used to determine a change of distance between bunch and radiator. At the investigated distances in the order of ≈ 1 mm we have seen that the photon yield changes exponentially with respect to the impact parameter, an effect which possibly could be applied in a highly sensitive BPM. Increasing the impact parameter to distances of several mm will reduce photon production significantly, however, the higher energy at FCC-ee and integration over several bunches may compensate for that. The studies at CLEAR have shown that the coherent part of the ChDR spectrum can be used to determine the beam position as well. Compared to incoherent ChDR, which scales linear with the number of particles, the coherent part of the spectrum has the advantage of scaling proportional to the number of particles squared. With the vast number of particles per bunch this results in a much higher signal.

In addition to this it has been demonstrated that the coherent part of the ChDR spectrum can be used to determine the bunch length with ps resolution. If the longitudinal profile is considered to be Gaussian at least two points in the frequency spectrum are required to estimate its bunch length. More points in frequency would allow for more elaborate profiles. Especially the high photon yield makes the coherent part of the spectrum a promising candidate for non-invasive bunch length measurements. However, to make use of this technique precise knowledge of the radiated energy spectrum of a single particle as well as a particle bunch is required. It is therefore key to study the radiated energy spectra of ChDR for the individual beam parameters of each machine and at the same time investigate and constrain the required parameter space for the measurements.

In the following chapters we introduce the formalism used for calculating the radiated energy spectra of ChDR from a single particle. For this we introduce different radiator geometries. Going from one particle to a particle bunch, we calculate the expected photon yield in the coherent and in the incoherent part of the spectrum for all the different operation modes of FCC-ee. We also have a closer look at the position sensitivity of BPMs operating with ChDR and the resolution of bunch length measurements.

2

Theory of Cherenkov diffraction radiation

2.1 Cherenkov radiation

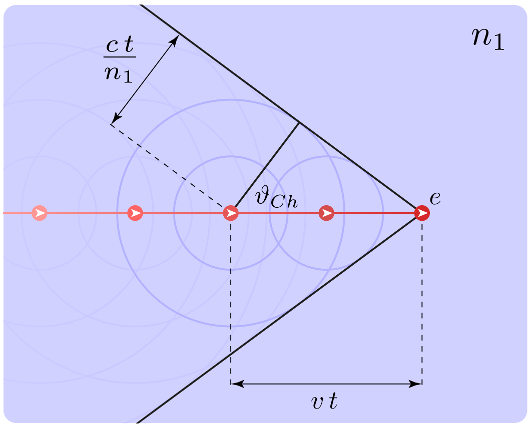

Figure 2.1: Illustration of the Cherenkov radiation principle. The wave front travels at an angle ϑ_{Ch} relative to the path of the charged particle.

A charged particle travelling through a dielectric medium faster than the phase velocity of light in the corresponding medium generates Cherenkov radiation [Che37]. With the charged particle moving uniformly in one direction it generates a wave front which forms a cone in three dimensions, or a pair of lines in two dimensions as shown in Fig. 2.1. The cosine of the angle ϑ_{Ch} is therefore equal to the ratio of the speed of light in the dielectric (v_{light}) divided by the speed of the charged particle ($v_{particle}$). With $v_{light} = c/n_1$ and $\beta = v_{particle}/c$ this leads to:

$$\cos(\vartheta_{Ch}) = \frac{1}{\beta\, n_1}, \tag{2.1}$$

where n_1 is the refractive index of the dielectric material and c is the speed of light in vacuum.

2.2 Cherenkov diffraction radiation

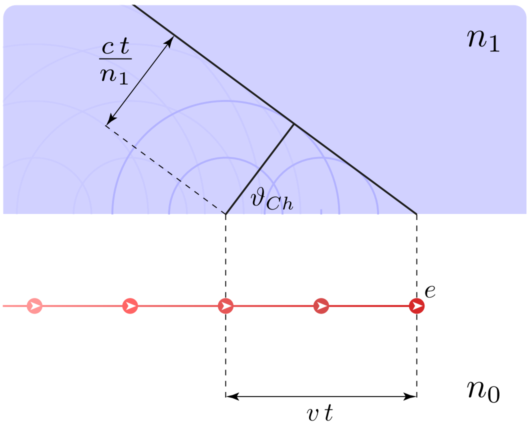

Figure 2.2: Illustration of the Cherenkov diffraction radiation principle. The wave front travels inside the dielectric at an angle ϑ_{Ch} relative to the path of the charged particle.

Cherenkov diffraction radiation (ChDR) on the other hand describes the same phenomenon for a charged particle just passing in the close vicinity of a dielectric material instead of travelling right through it. The light yield is considerably lower for ChDR than for ChR, nevertheless, its properties could be of great use in beam diagnostics.

The following two sections provide an introduction to the theoretical background of the simulations performed in this report. Using two different theoretical models the use of ChDR for beam instrumentation purposes has been investigated for cylindrical as well as flat geometries of radiators.

2.2.1 Cherenkov diffraction radiation in cylindrical geometries

In 1980 Olsen and Kolbenstvedt published their results on a study of Cherenkov radiation generated in one cylinder surrounded by dielectric. The geometry of their theoretical model is shown in Fig. 2.3a. By replacing the material of the inner cylinder with vacuum their model can be used for simulations of ChDR in beam diagnostics. The geometry used in this report is shown in Fig. 2.3b. The following paragraphs provide a summary of their work found in [OK80]. The presented summary is only considering the cases where the permittivity $\epsilon_2 > \epsilon_1$, whereas the inner medium with ϵ_1 will then be set to be vacuum. Note that Gaussian units are used and that notation has been changed in several parts compared to [OK80] to improve readability and comparability within this report.

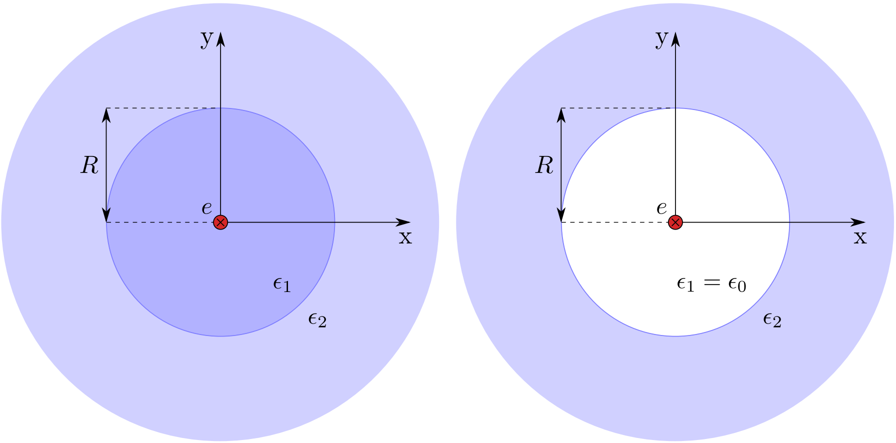

(a) Original model from Olsen and Kolbenstvedt.

(b) Use case for beam diagnostics.

Figure 2.3: Illustration of the difference between the cylindrical model in [OK80] and the used configuration for this report. Concentric layers of different dielectrics are shown in blue, the outer layer of dielectric extends to infinity. The electron is shown in red and travels along the axis perpendicular to the page.

To investigate the presented geometry we start with an electron travelling along the axis in the center of the cylinder. This electron yields the current density $\vec{j}(\vec{r},t) = e\,\vec{v}\,\delta(\vec{r}-\vec{v}t)$, with e being the elementary charge and $\vec{v}$ the constant velocity of the electron. δ denotes the Dirac delta function. The field generated by the particle satisfies the following equation for the vector potential $\vec{A}(\vec{r},t)$, where the Lorenz gauge condition for the vector potential is used:

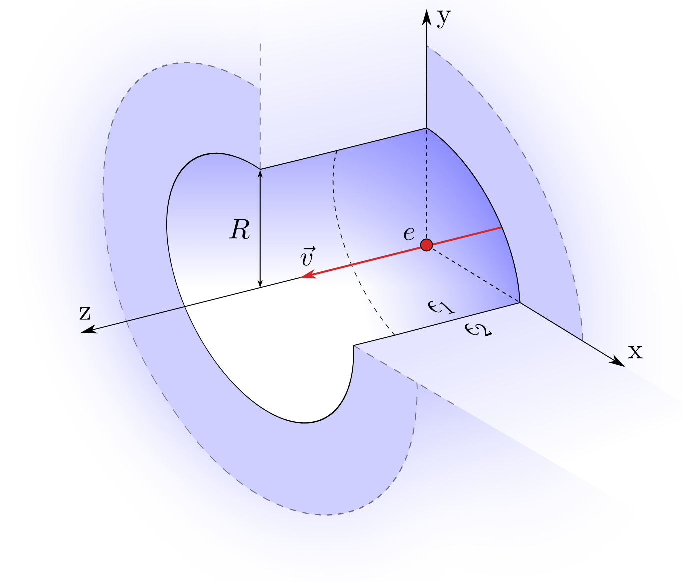

Figure 2.4: Illustration of the geometry used in the Cherenkov diffraction model by Olsen and Kolbenstvedt. The outer layer with permittivity ϵ_2 extends to infinity.

$$\nabla^2 \vec{A}(\vec{r},t) - \frac{\epsilon_r}{c^2}\frac{\partial^2}{\partial t^2}\vec{A}(\vec{r},t) = -\frac{4\pi}{c}\,\vec{j}(\vec{r},t), \tag{2.2}$$

where ϵ_r is the relative permittivity of the material and c the speed of light in vacuum. Using the Fourier transforms $\vec{A}(\vec{r},\omega) = \int e^{-i\omega t}\vec{A}(\vec{r},t)dt$ and $\vec{j}(\vec{r},\omega) = \int e^{-i\omega t}\vec{j}(\vec{r},t)dt$ we transform Eq. (2.2) and the current density $\vec{j}$ to the frequency domain where they are of the form

$$\left(\nabla^2 + k^2\right)\vec{A}(\vec{r},\omega) = -\frac{4\pi}{c}\,\vec{j}(\vec{r},\omega) \tag{2.3}$$

and

$$\vec{j}(\vec{r},\omega) = e\,\hat{v}\;\delta^2(\rho)\;\exp\left(i\frac{\omega}{v}z\right), \tag{2.4}$$

where $k^2 = \epsilon_r\left(\frac{\omega}{c}\right)^2$ and $\hat{v} = \frac{\vec{v}}{|\vec{v}|}$. The cylindrical coordinates ρ, ϕ, z are used, where z is set along the direction of propagation of the particle. Due to the form of Eq. (2.4) and Eq. (2.3) it is already evident that $\vec{A}(\vec{r},\omega)$ only has components in the z direction $A_z(\vec{r},\omega)$.

To find the particular solution of Eq. (2.3) the Green's function for cylindrical coordinates is used:

$$\begin{aligned} G(\vec{r}-\vec{r}\,') &= \frac{1}{4\pi}\frac{e^{ik|\vec{r}-\vec{r}\,'|}}{|\vec{r}-\vec{r}\,'|} \\ &= \frac{i}{8\pi}\sum_{m=\infty}^{\infty} e^{i\,m(\varphi-\varphi')} \times \\ &\quad \times \int_{-\infty}^{\infty} d\alpha\ J_m\left(\rho_< \cdot \sqrt{k^2-\alpha^2}\right)\ H_m^{(1)}\left(\rho_> \cdot \sqrt{k^2-\alpha^2}\right)\ e^{-i\,\alpha(z-z')}, \end{aligned} \tag{2.5}$$

where J_m and $H_m^{(1)}$ are the Bessel and Hankel functions of the first kind, and $\rho_<$ and $\rho_>$ correspond to the smaller and greater of ρ and ρ'. For the particular solution we are interested in cases which fulfill or do not fulfill the Cherenkov condition

$$\beta\, n = \beta\sqrt{\epsilon_r\mu_r} > 1. \tag{2.6}$$

As already presented in the Fig. 2.4 for the inner region we set $\epsilon_r = \epsilon_1$. The relative permeability is set to $\mu_r = 1$ for the inner and outer layer respectively. With the condition in Eq. (2.6) fulfilled the particular solution for the potential yields

$$\begin{aligned} A_z(\vec{r},\omega) &= \frac{4\pi e}{c}\int G(\vec{r}-\vec{r}\,')\ \delta^2(\rho')\ e^{i\frac{\omega}{v}z'}\ d^3x' \\ &= \frac{i\pi e}{c}\ H_0^{(1)}(\rho K_1)\ \exp\left(i\,\frac{\omega}{v}z\right), \end{aligned} \tag{2.7a}$$

where

$$K_{1/2} = \frac{\omega}{v}\sqrt{\epsilon_{1/2}\beta^2-1}.$$

For cases where Eq. (2.6) is not fulfilled in the inner region, the particular solution of the cylinder changes to:

$$A_z(\vec{r},\omega) = \frac{i\pi e}{c}\ H_0^{(1)}(i\rho\kappa_1)\ \exp\left(i\,\frac{\omega}{v}z\right) \tag{2.7b}$$

where

$$\kappa_1 = \frac{\omega}{v}\sqrt{1-\epsilon_1\beta^2}.$$

The total solution for Eq. (2.3) is then the sum of the homogeneous solution of Eq. (2.3) and one of the two solutions given in Eq. (2.7).

For the cases discussed in this report we are only interested in cases where the Cherenkov condition presented in Eq. (2.6) is valid only in the outer layer with $\epsilon_r = \epsilon_2$. So we constrain ourselves to $\beta\sqrt{\epsilon_1} < 1$ and $\beta\sqrt{\epsilon_2} > 1$. As shown, this results in

$$A_z(\vec{r},\omega) = \begin{cases} \frac{i\pi e}{c}\ \exp\left(i\,\frac{\omega}{v}z\right)\left[H_0^{(1)}(i\rho\kappa_1) + CJ_0(i\rho\kappa_1)\right], & \rho < R \quad (2.8a) \\ \frac{i\pi e}{c}\ \exp\left(i\,\frac{\omega}{v}z\right) DH_0^{(1)}(\rho K_2), & \rho > R \quad (2.8b) \end{cases}$$

where C and D are constants to be determined from the boundary conditions. To obtain the boundary conditions it is useful to note down the electric and magnetic fields in terms of $A_z(\vec{r},\omega)$ explicitly. The fields $\vec{E}(\vec{r},\omega)$ and $\vec{H}(\vec{r},\omega)$ are given in the frequency domain as

$$\begin{aligned} \vec{E}(\vec{r},\omega) &= \frac{ic}{\omega\epsilon_r}\nabla\left[\nabla\vec{A}(\vec{r},\omega)\right] + \frac{i\omega}{c}\vec{A}(\vec{r},\omega), \\ \vec{H}(\vec{r},\omega) &= \nabla\times\vec{A}(\vec{r},\omega), \end{aligned}$$

whereas only the following components are non-zero:

$$\begin{aligned} E_\rho(\vec{r},\omega) &= \frac{1}{\beta\epsilon_r}\,\frac{\partial}{\partial\rho}A_z(\vec{r},\omega), \\ E_z(\vec{r},\omega) &= \frac{i\omega}{c}\left(1-\frac{1}{\beta^2\epsilon_r}\right)A_z(\vec{r},\omega), \qquad (2.9) \\ H_\varphi(\vec{r},\omega) &= -\frac{\partial}{\partial\rho}A_z(\vec{r},\omega), \end{aligned}$$

where $\epsilon_r = \epsilon_1$ for $\rho < R$ and $\epsilon_r = \epsilon_2$ for $\rho > R$. The boundary conditions at $\rho = R$ are satisfied for $\frac{\partial}{\partial\rho} A_z(\vec{r}, \omega)$ and $(1 - \frac{1}{\beta^2 \epsilon}) A_z(\vec{r}, \omega)$ continuous. These two boundary conditions together with 2.8a and 2.8b determine the constants C and D:

$$C = \frac{R}{N} \left(i\kappa_1 \frac{\epsilon_2}{\epsilon_1} \cdot H_0^{(1)}(iR\kappa_1) \cdot H_1^{(1)}(RK_2) - K_2 \cdot H_0^{(1)}(RK_2) \cdot H_1^{(1)}(iR\kappa_1) \right) \tag{2.10}$$

$$\text{and} \quad D = -\frac{2}{\pi N} \frac{\epsilon_2 \, \kappa_1}{\epsilon_1 \, K_2}, \tag{2.11}$$

with

$$N = RK_2 \cdot H_0^{(1)}(RK_2) \cdot J_1(iR\kappa_1) - iR\kappa_1 \frac{\epsilon_2}{\epsilon_1} \cdot J_0(iR\kappa_1) \cdot H_1^{(1)}(RK_2).$$

The energy radiated in the radial direction per unit length of the cylinder dW/dl is obtained from the Poynting vector $\vec{S} = \frac{c}{4\pi} \vec{E} \times \vec{H}$ and yields

$$\frac{dW}{dl} = 2\pi\rho \int_{-\infty}^{\infty} S_\rho(\vec{r}, t) dt, \tag{2.12}$$

with S_ρ denoting the Poynting vector in any arbitrary point located at the distance ρ perpendicular to the axis. Transforming this into frequency domain and considering Eq. (2.9) yields

$$\frac{dW}{dl} = \frac{c\rho}{4\pi} \int_0^{\infty} \left[E_z(\vec{r}, \omega) H_\varphi(\vec{r}, -\omega) + E_z(\vec{r}, -\omega) H_\varphi(\vec{r}, \omega) \right] d\omega. \tag{2.13}$$

For the outer layer with $\rho > R$ inserting Eq. (2.8) into Eq. (2.9) leads to the final result:

$$\frac{dW}{dl} = \frac{e^2}{c^2} \int_0^{\infty} \omega \left(1 - \frac{1}{\beta^2 n^2(\omega)} \right) |D|^2 \, d\omega. \tag{2.14}$$

Comparing this to the Frank-Tamm equation in Gaussian units [FT37, Tam39], which is given as

$$\frac{dW}{dl} = \frac{e^2}{c^2} \int_0^{\infty} \omega \left(1 - \frac{1}{\beta^2 n^2(\omega)} \right) d\omega, \tag{2.15}$$

shows that for $D = 1$ the result obtained by Olsen and Kolbenstvedt yields the Frank-Tamm equation.

2.2.2 Cherenkov diffraction radiation in flat geometries

In 1966 Ulrich studied the Cherenkov radiation emitted from an electron moving parallel to the surface of a flat dielectric material. Its surface expands infinitely in both directions and the dielectric is infinitely thick as illustrated in Fig. 2.7. The following paragraphs provide a brief overview of his work with a focus on the results relevant for this report. Note that Gaussian units are used and notation is changed in several parts compared to [Ulr66] to improve readability and comparability within this report.

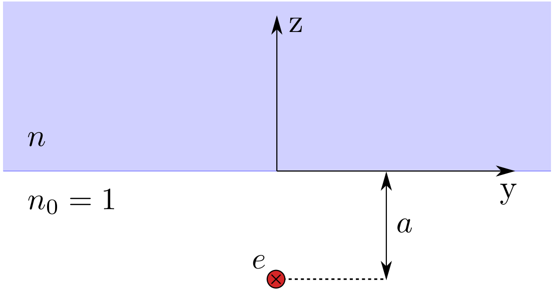

Figure 2.5: Illustration of the flat model of Ulrich in the transverse plane. The electron is shown in red and travels perpendicular to the page.

An electron travelling parallel along the surface of a flat dielectric with a constant velocity v has the coordinates $x(t) = vt$, $y(t) = 0$, $z(t) = -a$, where a is the distance to the surface and $a > 0$ for the discussed cases. In vacuum the electric and magnetic fields generated by the electron can be described as superposition of plane waves attenuated in the transverse direction:

$$\vec{E}(\vec{r}, t) = \sum_{j=1,2} \int_{-\infty}^{+\infty} dk \int_{-\infty}^{+\infty} dq \; A_j(k, q) \vec{E}_j(k, q; \vec{r}, t), \tag{2.16}$$

$$\vec{H}(\vec{r}, t) = \sum_{j=1,2} \int_{-\infty}^{+\infty} dk \int_{-\infty}^{+\infty} dq \; A_j(k, q) \vec{H}_j(k, q; \vec{r}, t). \tag{2.17}$$

Index $j = 1$ corresponds to TM polarized and $j = 2$ to TE polarized waves.

$$\begin{aligned} \vec{E}_1(k, q; \vec{r}, t) &= -\begin{pmatrix} isp \\ isq \\ p^2+q^2 \end{pmatrix} \exp\Big(ik(ct - px - qy) - ksz\Big), \\ \vec{E}_2(k, q; \vec{r}, t) &= \begin{pmatrix} q \\ -p \\ 0 \end{pmatrix} \exp\Big(ik(ct - px - qy) - ksz\Big), \end{aligned} \tag{2.18a}$$

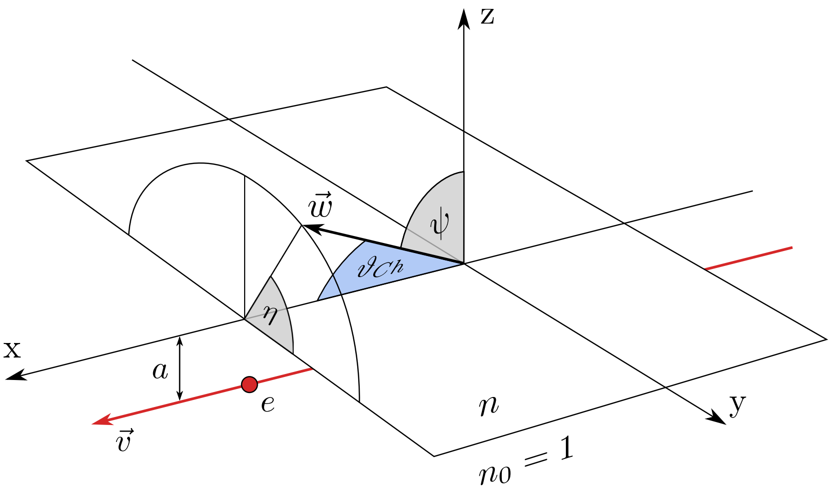

Figure 2.6: Illustration of the flat model of Ulrich introducing the angular dependencies of the unit vector $\vec{w}$ in the direction of propagation of ChDR.

$$\begin{aligned}\vec{H}_1(k,q;\vec{r},t) &= \begin{pmatrix} -q \\ p \\ 0 \end{pmatrix} \exp\Big(ik(ct-px-qy)-ksz\Big),\\ \vec{H}_2(k,q;\vec{r},t) &= -\begin{pmatrix} isp \\ isq \\ p^2+q^2 \end{pmatrix} \exp\Big(ik(ct-px-qy)-ksz\Big),\end{aligned} \tag{2.18b}$$

where $k = \omega/c$ parameterises the waves regarding frequency and p, q regarding direction of propagation. We take $s = \pm\sqrt{p^2+q^2-1}$ and k, p, q real, whereas the sign of s has to be chosen in such a way, that $k \cdot s > 0$ to ensure the damping increases in the positive z direction.

As shown in [TdF60], we have $p = 1/\beta$, and one obtains for the amplitudes in Eqs. (2.16) and (2.17)

$$\begin{aligned}A_1(k,q) &= -\frac{e|k|}{2\pi}\,\frac{\beta}{1+\beta^2q^2}\cdot e^{-a|k|\sqrt{q^2+\beta^{-2}-1}},\\ A_2(k,q) &= -\frac{iek}{2\pi}\,\frac{\beta^2 q}{(1+\beta^2q^2)\sqrt{q^2+\beta^{-2}-1}}\cdot e^{-a|k|\sqrt{q^2+\beta^{-2}-1}}.\end{aligned} \tag{2.19}$$

The elementary waves in Eq. (2.18) may hit the surface of the dielectric at $z = 0$ and be partly reflected as well as refracted. With the unit vector $\vec{w} = (p', q', s')$ we use the following ansatz for the refracted waves:

$$\begin{aligned}\vec{E}_1'(k,q;\vec{r},t) &= n\begin{pmatrix} p's' \\ q's' \\ -(p'^2+q'^2)\end{pmatrix} e^{ik(ct-np'x-nq'y-ns'z)},\\ \vec{E}_2'(k,q;\vec{r},t) &= n\begin{pmatrix} q' \\ -p' \\ 0\end{pmatrix} e^{ik(ct-np'x-nq'y-ns'z)},\end{aligned} \tag{2.20a}$$

$$\begin{aligned}\vec{H}_1'(k,q;\vec{r},t) &= n^2\begin{pmatrix} -q' \\ p' \\ 0\end{pmatrix} e^{ik(ct-np'x-nq'y-ns'z)},\\ \vec{H}_2'(k,q;\vec{r},t) &= n^2\begin{pmatrix} p's' \\ q's' \\ -(p'^2+q'^2)\end{pmatrix} e^{ik(ct-np'x-nq'y-ns'z)},\end{aligned} \tag{2.20b}$$

where n is the refractive index of the dielectric. With the help of a similar second set of equations for the reflected waves and the boundary conditions for the fields at the surface $z = 0$ one can obtain the transmission coefficients T_1 and T_2 and the relations between the parameters p', q' and s' and their counterparts in the unfractured area:

$$T_1(q) = \frac{2\,s(q)}{n\,s(q) + i\,s'(q)} \quad \text{and} \quad T_2(q) = \frac{2\,s(q)}{s(q) + in\,s'(q)}, \tag{2.21}$$

$$p' = \frac{p}{n} = \frac{1}{\beta n}, \tag{2.22a}$$

$$q' = \frac{q}{n}, \tag{2.22b}$$

$$s' = \frac{1}{n}\sqrt{n^2 - p^2 - q^2} = \frac{1}{n}\sqrt{n^2 - \frac{1}{\beta^2} - q^2}\,. \tag{2.22c}$$

In order for the refracted waves not to be damped, p', q' and s' have to be real. According to Eq. (2.22c) this can only be the case for $\frac{1}{\beta n} < 1$ which is equal to the Cherenkov condition already introduced in Eq. (2.6). From Eq. (2.22) one can also observe that the angle between the x-axis and the direction of propagation of the refracted wave is $\vartheta = \arccos(\frac{1}{\beta n})$ which is equal to the Cherenkov angle introduced in Eq. (2.1). The fields of the refracted electromagnetic waves are superpositions of the waves in Eq. (2.20) attenuated by the transmission coefficients:

$$\vec{E}'(\vec{r},t) = \sum_{j=1,2}\int_{-\infty}^{+\infty} dk \int_{-\infty}^{+\infty} dq\; A_j(k,q)\,T_j(q)\,\vec{E}_j'(k,q;\vec{r},t), \tag{2.23}$$

$$\vec{H}'(\vec{r},t) = \sum_{j=1,2} \int_{-\infty}^{+\infty} dk \int_{-\infty}^{+\infty} dq\ A_j(k,q)\, T_j(q)\, \vec{H}_j'(k,q;\vec{r},t). \tag{2.24}$$

Next we calculate the fields for a point in the dielectric with the coordinates $x = 0$, $y = \rho\,\cos(\eta)$ and $z = \rho\,\sin(\eta)$. For a plane wave to contribute to the fields, the unit vector in the direction of propagation $\vec{w} = (p', q', s')$ has to be real. We parameterise q' and s' with the help of η which leads to $\vec{w} = (p', q'(q_0), s'(q_0))$ with $q_0 = \sqrt{n^2 - \frac{1}{\beta^2}}\,\cos(\eta)$ and p', q' and s' from Eq. (2.22).

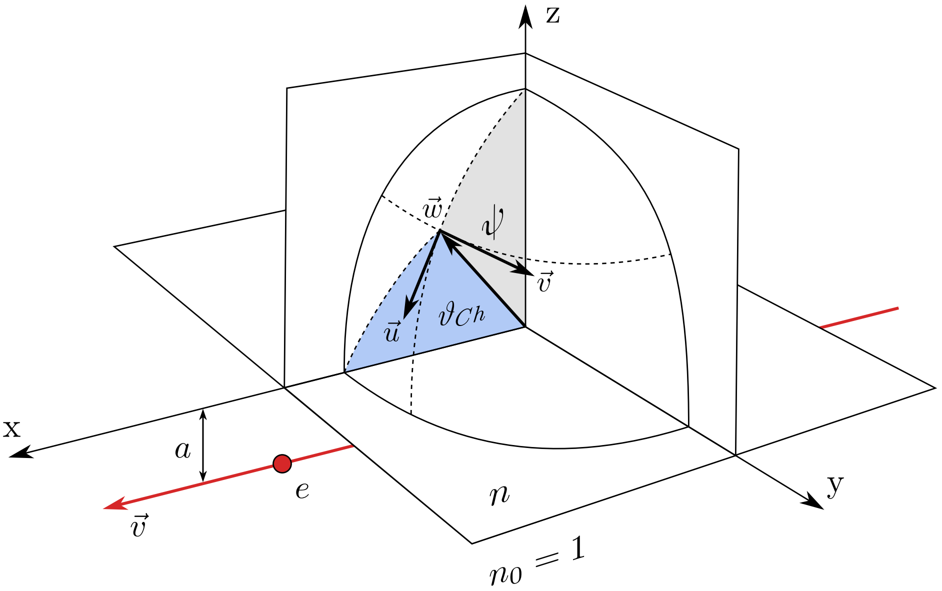

Figure 2.7: Illustration of the flat model of Ulrich introducing the vectors $\vec{u}$ and $\vec{v}$. The unit vector $\vec{w}$, the Cherenkov angle ϑ_{Ch} and the angle ψ have already been introduced in Fig. 2.6.

With $n = \textit{constant}$ the electric and magnetic fields are always in the plane perpendicular to the unit vector $\vec{w}$. This plane is generated by the two vectors $\vec{u}$ and $\vec{v}$ as shown in Fig. 2.7, therefore:

$$\begin{aligned} \vec{E}'\left(\begin{pmatrix} 0 \\ \rho\,\cos(\eta) \\ \rho\,\sin(\eta) \end{pmatrix}, t\right) &= \vec{u}\,B_1 - \vec{v}\,B_2, \\ \vec{H}'\left(\begin{pmatrix} 0 \\ \rho\,\cos(\eta) \\ \rho\,\sin(\eta) \end{pmatrix}, t\right) &= \vec{v}\,n\,B_1 - \vec{u}\,n\,B_2, \end{aligned} \tag{2.25}$$

$$\text{where} \quad \vec{u} = \begin{pmatrix} p'\,s'(q_0) \\ q'\,s'(q_0) \\ -[p'^2+q'^2(q_0)] \end{pmatrix} \quad \text{and} \quad \vec{v} = \begin{pmatrix} -q'(q_0) \\ p' \\ 0 \end{pmatrix}.$$

The amplitudes in Eq. (2.25) are given as

$$B_j = \int_0^\infty dk\ 2\,n\,\sin(\eta)\sqrt{2\pi\,n\,k\,\rho\,\sin(\vartheta_{Ch})}\ \ |T_j(q_0)|\ \ |A_j(k,q_0)|\ \ \cos(\varphi_j),$$

with

$$\varphi_j(k,q_0) = k\,c\,t - n\,k\,\rho\,\sin(\vartheta_{Ch}) + \alpha_j(q_0) + \tau_j(q_0) + \pi/4,$$

whereas α_j are the phases of the Fourier coefficients

$$\alpha_1 = \pi, \quad \alpha_2 = \begin{cases} -\pi/2, & 0 \leq \eta < \pi/2 \\ +\pi/2, & \pi/2 < \eta \leq \pi \end{cases}$$

and τ_j are the phases of the transmission coefficients $T_j = |T_j|\,e^{i\,\tau_j}$. With $s'(q_0) = \cos(\psi)$ and the transmission coefficients in Eq. (2.21) we obtain

$$|T_1(q_0)|^2 = \frac{4}{n^2}\,\frac{1-\frac{n^2}{n^2-1}\cos^2(\psi)}{1-\frac{n^2+1}{n^2}\cos^2(\psi)}\,, \quad |T_2(q_0)|^2 = 4\left(1-\frac{n^2}{n^2-1}\cos^2(\psi)\right) \tag{2.27}$$

and

$$\tan(\tau_1(q_0)) = \mp\frac{1}{n}\,\frac{\cos(\psi)}{\sqrt{n^2\sin^2(\psi)-1}}\,, \quad \tan(\tau_2(q_0)) = \mp\,n\,\frac{\cos(\psi)}{\sqrt{n^2\sin^2(\psi)-1}},$$

where the minus sign applies to $k > 0$ and the plus sign to $k < 0$.

Now we can finally calculate the Poynting vector $\vec{S} = \frac{c}{4\pi}\,\vec{E}\times\vec{H}$ to obtain the directional energy flux due to Cherenkov diffraction radiation. With the help of Eq. (2.25) the Poynting vector becomes

$$\begin{aligned} \vec{S} &= \vec{S}_1 + \vec{S}_2, \\ \vec{S} &= \frac{n\,c}{4\pi}\,\sin^2(\psi)\left(B_1^2 + B_2^2\right)\vec{w}. \end{aligned} \tag{2.28}$$

As we are interested in the spectral distribution of the radiated energy we need to integrate the energy flux over time. Therefore we consider a cylinder of radius ρ with surface elements $d\vec{f} = \rho \, d\eta \, dl \, (0, \cos(\eta), \sin(\eta))$. For each polarisation of the Poynting vector the energy radiated per unit length l and azimuth angle η is

$$\begin{aligned} \frac{dW_j}{dl \, d\eta} &= \int_{-\infty}^{+\infty} dt \; \frac{n \, c}{4\pi} \; \sin^2(\psi) \sin(\vartheta_{Ch}) B_j^2 \\ &= \int_{-\infty}^{+\infty} dt \int_0^{\infty} dk \int_0^{\infty} dk' \; 2n^4 \, c \sqrt{kk'} \; \sin^2\psi \; \cos^2\psi \; |T_j|^2 \; \times \\ &\qquad\qquad \times |A_j(k)| \; |A_j(k')| \; \cos(\varphi_j(k)) \; \cos(\varphi_j(k')). \end{aligned}$$

After integration over t and k' this yields

$$\frac{dW_j}{dl \, d\eta} = \int_0^{\infty} dk \; 2\pi \, n^4 \; \sin^2\psi \; \cos^2\psi \; |T_j|^2 \; |A_j(k)|^2. \tag{2.29}$$

The integrand of Eq. (2.29) is the desired distribution, which after using the angular frequency ω instead of the wavenumber k can be written as

$$\frac{dW_j}{dl \, d\eta \, d\omega} = \frac{2\pi}{\omega} n^4 \; \sin^2\psi \; \cos^2\psi \; |T_j|^2 \; |A_j|^2. \tag{2.30}$$

After inserting the expressions for $|T_j|$ and $|A_j|$ as seen in Eq. (2.27) and Eq. (2.19), as well as expressing all angles with the help of η and $\vartheta_{Ch} = \arccos(\frac{1}{\beta \, n})$ the final energy distribution yields

$$\frac{dW_j}{dl \, d\eta \, d\omega} = \frac{e^2}{2\pi c^2} \cdot \omega \cdot F_j \cdot \exp\left(-2 \, \frac{\omega}{c} \, a \, \kappa\right), \tag{2.31}$$

with the factors F_j describing the azimuth distribution for the TM and TE waves respectively:

$$F_1(n,\beta,\eta) = 4\,\frac{\sin^2(\vartheta_{Ch})\,\cos^2(\vartheta_{Ch})\,\sin^2(\eta)}{1-\sin^2(\vartheta_{Ch})\,\sin^2(\eta)}\;\frac{1-\dfrac{n^2}{n^2-1}\sin^2(\vartheta_{Ch})\sin^2(\eta)}{1-\dfrac{n^2+1}{n^2}\sin^2(\vartheta_{Ch})\sin^2(\eta)}\,,$$

$$F_2(n,\beta,\eta) = \frac{4\,n^2}{n^2-1}\;\frac{\sin^4(\vartheta_{Ch})\,\sin^2(\eta)\,\cos^2(\eta)}{1-\sin^2(\vartheta_{Ch})\,\sin^2(\eta)}\,.$$

The factor κ in the exponent is given as

$$\begin{aligned}\kappa(n,\beta,\eta) &= \sqrt{n^2-1-n^2\sin^2(\vartheta_{Ch})\sin^2(\eta)}\\ &= \sqrt{n^2\cos^2(\eta)+\frac{\sin^2(\eta)}{\beta^2}-1}\,.\end{aligned}$$

For a particle passing through bulk material the radiation is isotropic with respect to η and the impact parameter a is of course 0. The factor F in Eq. (2.31) then can be described as $\sin^2(\vartheta_{Ch})$ and the exponential function becomes 1. Using the identity $\sin^2(\arccos(x)) = 1 - x^2$ and Eq. (2.1) for the Cherenkov angle ϑ_{Ch} it can be shown that

$$\sin^2(\vartheta_{Ch}) = 1 - \frac{1}{\beta^2 n^2(\omega)}\,.$$

So for a particle passing through bulk material Eq. (2.31) resembles Frank-Tamm equation.

In general the factors F_j in Eq. (2.31) both are proportional to $\sin^2(\vartheta_{Ch})$ and describe the $\eta-$dependency caused by the flat geometry. The exponential function has no contribution for $a = 0$. Moreover, only for wavelengths $\lambda \lessapprox a$ the radiated energy reduces compared to Frank-Tamm. For wavelengths $\lambda \gg a$ the impact parameter has a negligible effect and the spectrum behaves like $a \to 0$.

Gaussian to SI units

Whereas Gaussian units have turned out to be of great use for the calculations in the previous sections 2.2.1 and 2.2.2 in all other parts of this report SI units are used. Therefore the conversion from Gaussian to SI units is given here to provide the link between these two sections and the rest of the report. As the final equations in the sections 2.2.1 and 2.2.2, namely Eqs. (2.14) and (2.31) are modifying the Frank-Tamm formula in such a way, that a dimensionless factor is added, it is sufficient to only have a closer look at the Frank-Tamm formula itself to introduce the desired conversion.

Frank-Tamm formula
in Gaussian units:

$$\frac{dW}{dl\,d\omega} = \frac{(q^G)^2}{c^2} \cdot \omega \cdot \left(1 - \frac{1}{\beta^2 n^2(\omega)}\right) \tag{2.32}$$

where W, l and q^G are given in $[erg], [cm]$ and $[statC]$ respectively. Here q^G denotes the electrical charge in Gaussian units. Note that β and n are dimensionless. To obtain our result in SI units we use the conversion factor between q^G and q, which is given as $\frac{q^G}{q} = \frac{1}{\sqrt{4\pi\epsilon_0}}$. Then with $c = \frac{1}{\sqrt{\epsilon_0\mu_0}}$ Eq. (2.32) can be written in the form

Frank-Tamm formula
in SI units:

$$\frac{dW}{dl\,d\omega} = \frac{q^2}{4\pi} \cdot \mu_0 \cdot \omega \cdot \left(1 - \frac{1}{\beta^2 n^2(\omega)}\right)$$

where all variables are given in SI units. As a result W, l, ω are given in $[J], [m]$ and $[1/s]$ respectively, q is given in $[C]$ and μ_0 is the vacuum permeability in $[H/m]$.

2.3 Bunch spectrum and form factor

The previous sections 2.2.1 and 2.2.2 provide a theoretical model of the radiated energy spectrum of the radiation produced by an electron moving in the vicinity of dielectric material of various geometric shapes. The aim of this section is to use the obtained results and apply them to a special experimental case, namely going from a single particle to multiple particles forming an electron bunch. The derivation follows the approach presented in [GDHR$^+$08] by Grimm et al. and [GS06] by Grimm and Schmüser.

The electric field of N electrons in a bunch is given as a superposition of their individual field contributions. For brevity we suppress the variable $\vec{r}$ and therefore define $\vec{E}(\vec{r},t) \equiv \vec{E}(t)$. We disregard any transverse displacement of particles, leaving only the longitudinal dimension, equivalent to time. Moreover, we are considering the field at a fixed observation point. The superposition of the fields is

$$\vec{E}(t) = \sum_{i=1}^{N} \vec{E}_i(t). \tag{2.33}$$

To obtain the spectrum in frequency domain we use the Fourier transform $\vec{E}(\omega) = \int_{-\infty}^{\infty} \vec{E}(t)\ e^{-i\omega t}dt$. We suppose that the contribution from each particle is the same except for time-delays due to their spatial offset from the reference particle 1. If the field of the reference particle is given as $\vec{E}_1(t)$, then the field of any particle i will be given as $\vec{E}_i(t) = \vec{E}_1(t + \Delta t_i)$, whereas Δt_i is a time delay of a particle i with respect to the reference particle. The total field in Eq. (2.33) in frequency domain is then given as

$$\begin{aligned}
\vec{E}(\omega) &= \int_{-\infty}^{\infty} \sum_{i=1}^{N} \vec{E}_i(t)\, e^{-i\omega t}dt = \sum_{i=1}^{N} \int_{-\infty}^{\infty} \vec{E}_1(t + \Delta t_i')\, e^{-i\omega t}dt \\
&= \sum_{i=1}^{N} \int_{-\infty}^{\infty} \vec{E}_1(t)\, e^{-i\omega(t-\Delta t_i')}dt = \sum_{i=1}^{N} e^{i\omega \Delta t_i'} \int_{-\infty}^{\infty} \vec{E}_1(t)\, e^{-i\omega(t-\Delta t_i')}dt \\
&= \sum_{i=1}^{N} e^{i\omega \Delta t_i'}\ \vec{E}_1(\omega).
\end{aligned} \tag{2.34}$$

Next we express the time difference $\Delta t_i'$ in terms of the wave vector $\vec{k}$, which is pointing from the reference particle to the observation point and the vector $\vec{r}_i$, which represents the spatial vector from the reference particle 1 to any particle i.

For this we assume that the spatial distance between the reference particle and the point of observation is much larger than the spatial distances between the individual particles. We have

$$\Delta t_i = -\frac{\vec{k} \cdot \vec{r}_i}{|\vec{k}|\, c}, \tag{2.35}$$

with $\vec{k}$ given as

$$\vec{k} = \frac{2\pi}{\lambda}\vec{n} = \frac{\omega}{c}\vec{n} \tag{2.36}$$

and $\vec{n}$ pointing from the reference particle to the observation point. So the time delay Δt_i leads to a phase shift of $-\vec{k} \cdot \vec{r}_i$ between the waves emitted from particle i and particle 1.

The derivation of the energy density spectrum is given in Appendix A of [GS06] and yields

$$\frac{d^2W}{dA\, d\lambda} = \frac{2\epsilon_0 c^2}{\lambda^2} \left\langle \left|\vec{E}(\vec{k})\right|^2 \right\rangle, \tag{2.37}$$

with energy W and area A. The angle brackets indicate that the ensemble average must be taken into account for the macroscopic quantity $\frac{d^2W}{dA\, d\lambda}$ as $\vec{E}(\vec{k})$ yields from one particular microscopic distribution. Inserting Eqs. (2.34) and (2.35) yields

$$\begin{aligned} \frac{d^2W}{dA\, d\lambda} &= \frac{2\epsilon_0 c^2}{\lambda^2} \left\langle \left|\sum_{i=1}^{N} e^{-i\vec{k}\cdot\vec{r}_i}\ \vec{E}_1(\vec{k})\right|^2 \right\rangle \\ &:= \left(\frac{d^2W}{dA\, d\lambda}\right)_1 \cdot \left\langle \left|\sum_{i=1}^{N} e^{-i\vec{k}\cdot\vec{r}_i}\right|^2 \right\rangle, \end{aligned} \tag{2.38}$$

with $(\frac{d^2W}{dA\, d\lambda})_1$ being the radiated energy spectrum of a single particle. The ensemble average can be rearranged to

$$\begin{aligned}
\left\langle \left| \sum_{i=1}^{N} e^{-i\vec{k}\cdot\vec{r}_i} \right|^2 \right\rangle &= \left\langle \left(\sum_i e^{-i\vec{k}\cdot\vec{r}_i} \right) \cdot \left(\sum_j e^{i\vec{k}\cdot\vec{r}_j} \right) \right\rangle \\
&= \sum_{i=1}^{N} 1 + \left\langle \sum_{i=1}^{N} \sum_{\substack{j=1 \\ j\neq i}}^{N} e^{-i\vec{k}\cdot\vec{r}_i} \cdot e^{i\vec{k}\cdot\vec{r}_j} \right\rangle \qquad (2.39) \\
&= N + \left\langle \sum_{i=1}^{N} e^{-i\vec{k}\cdot\vec{r}_i} \right\rangle \left\langle \sum_{\substack{j=1 \\ j\neq i}}^{N} e^{i\vec{k}\cdot\vec{r}_j} \right\rangle .
\end{aligned}$$

Now we introduce the normalized three-dimensional particle density distribution

$$S_{3D}(\vec{r}) = \frac{1}{N} \left\langle \sum_{i=1}^{N} \delta(\vec{r} - \vec{r}_i) \right\rangle = \frac{1}{N-1} \left\langle \sum_{\substack{j=1 \\ j\neq i}}^{N} \delta(\vec{r} - \vec{r}_j) \right\rangle , \qquad (2.40)$$

whereas the two averages are equal because of the assumption of uncorrelated particles. Now we can rewrite Eq. (2.38) to

$$\frac{d^2W}{dA\,d\lambda} = \left(\frac{d^2W}{dA\,d\lambda} \right)_1 \cdot \left(N + N\big(N-1\big) \int S_{3D}(\vec{r}) e^{-i\vec{k}\,\vec{r}} d\vec{r} \int S_{3D}(\vec{r'}) e^{i\vec{k}\,\vec{r'}} d\vec{r'} \right) . \qquad (2.41)$$

As the three-dimensional bunch form factor is defined as the Fourier transform of the three-dimensional particle density distribution

$$F_{3D}(\vec{k}) = \int S_{3D}(\vec{r}) e^{-i\vec{k}\,\vec{r}} d\vec{r}, \qquad (2.42)$$

we obtain our final result as

$$\frac{d^2W}{dA\,d\lambda} = \left(\frac{d^2W}{dA\,d\lambda} \right)_1 \cdot \left(N + N\big(N-1\big) \cdot \left| F_{3D}(\vec{k}) \right|^2 \right) . \qquad (2.43)$$

The first term in Eq. (2.43) is the intensity obtained when the N particles emit independently from each other so that intensities are added, not the amplitudes. This is the incoherent part of the spectrum. The second part takes the phase relations among the N particles into account, forming the coherent part of the spectrum [LS96].

As the equations for the radiated energy due to Cherenkov diffraction radiation in the previous sections partly are given with respect to the wavelength λ and partly with respect to the angular frequency ω we also provide the conversion between the two of them. As we require

$$\left|\frac{dW}{d\omega}d\omega\right| = \left|\frac{dW}{d\lambda}d\lambda\right|, \tag{2.44}$$

we obtain

$$\frac{dW}{d\lambda} = \frac{\omega^2}{2\pi c}\,\frac{dW}{d\omega}\,. \tag{2.45}$$

3

Applications of ChDR

3.1 Simulation parameters

3.1.1 Dielectric function

The relative permittivity of any material is a function of frequency. The dielectric function describes this dependency. The dielectric function of fused silica (SiO_2) shown in Fig. 3.1 was used in the simulations, where the material SiO_2 is indicated. As already shown in Eq. (2.1) the Cherenkov angle ϑ_{Ch} depends on the particles velocity v and the refractive index n of the material. As ϵ_r of SiO_2 is different in different regimes of the spectrum also the Cherenkov angle changes. With $v \approx c$ and the values provided in Fig. 3.1 we obtain for the GHz range $\vartheta_{Ch} \approx 59.2°$ and for the visible spectrum $\vartheta_{Ch} \approx 46.7°$.

Often we are only interested in a particular range of the relative permittivity of a specific material. If this range is narrow and far from resonances (as can be seen between 10^{13} and 10^{14} Hz in Fig. 3.1) the relative permittivity can be assumed to be constant in that range. In calculations where a constant value for the relative permittivity has been used, it is explicitly mentioned and taken from [Pol20], where a library of various parameters for a wide range of materials is provided.

3.1.2 Geometry considerations

To improve the comparison between the two presented models also in quantitative numbers, the calculated radiated energy spectrum of the cylindrical geometry is scaled down to only a fraction of the full circle for most simulations. This is illustrated in Fig. 3.2. If not stated otherwise the total angle ($2 \times \alpha$ in Fig. 3.2)

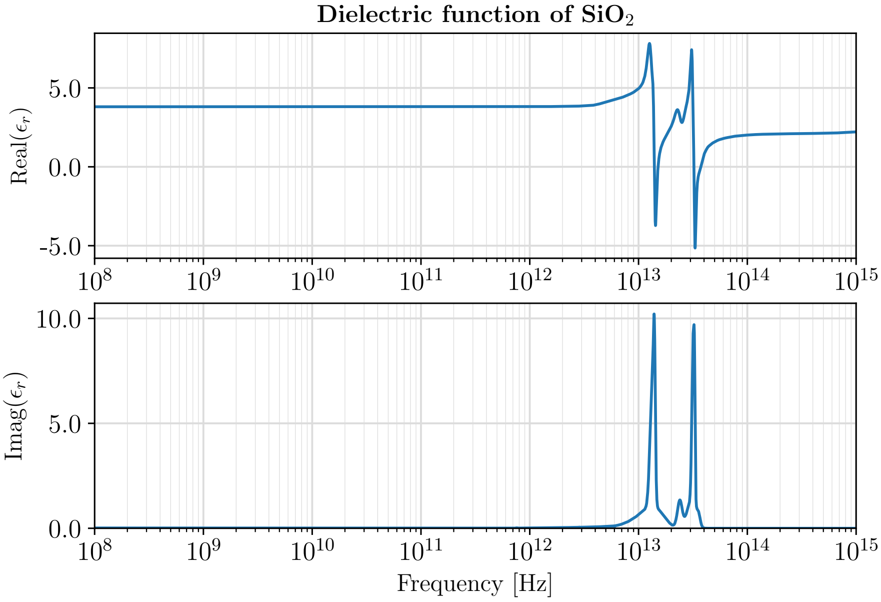

Figure 3.1: Real and imaginary part of the relative permittivity ϵ_r of SiO$_2$ [KPJ07]. Due to the lack of available data for frequencies lower than 6.3×10^{11} Hz the relative permittivity is assumed to stay constant for these frequencies.

was chosen to be 60°, denoted as Cylindrical (60°) in various plots. On top of that the calculations often are scaled down to a shorter radiator length, denoted as l. As a standard value in the presented calculations a radiator length of 10 mm was chosen.

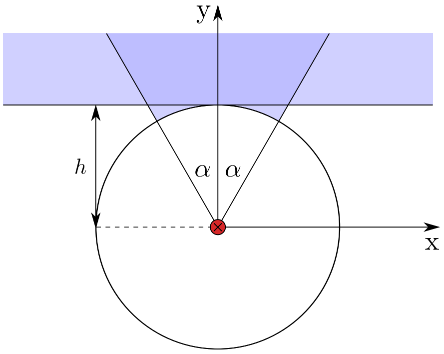

Figure 3.2: Illustration of the two considered geometries. The particle is shown in red and travels perpendicular to the page at a distance of h. Only a fraction of the cylindrical geometry is considered in order to obtain comparable results in quantitative numbers.

3.2 Single particle spectrum

As we have seen in Eq. (2.43), the radiated energy spectrum of the single particle together with the bunch form factor and the number of particles in the bunch will yield the radiated energy spectrum of a bunch in the end. So before analyzing the spectra resulting from the different bunches, each consisting of a large number of electrons, it is useful to have a closer look at the radiated energy spectrum of a single particle first. In chapter 2 two theoretical models have been introduced to describe the radiated energy spectrum of a single particle. The resulting radiated energy spectra of a single particle are presented in Fig. 3.3. To show the general behaviour of the functions independent of a change in $\epsilon_r(\omega)$ with respect to frequency, the relative permittivity ϵ_r is considered a constant in this section. The value $\epsilon_r = 3.8$ was chosen for these plots, which is approximately the relative permittivity of fused silica (SiO_2) in the low THz range as seen in Fig. 3.1. Note that in the current section the data is not scaled, therefore the length of the considered radiator is $l = 1000$ mm and for the cylindrical geometry a full circle of 360° is considered.

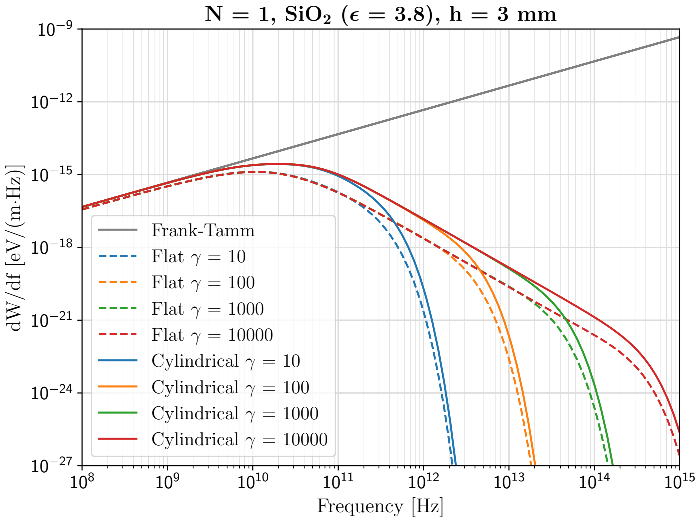

Figure 3.3: Radiated energy spectrum of a single particle for flat and cylindrical geometry for different values of γ.

In Fig. 3.3 we can observe three different regimes in the spectrum for each value of γ. First the spectrum increases $\propto \omega$, just as it does in the Frank-Tamm theory. For frequencies which correspond to a wavelength in a similar order of magnitude as the impact parameter, the spectrum does not follow the linear dependency in ω anymore. This is to be expected as for low frequencies (longer wavelengths) the influence of the impact parameter should be neglectable for wavelengths greater than the impact parameter and the spectrum therefore approaches the Frank-Tamm behaviour.

The second part of the spectrum decreases $\propto \omega^{-2}$, which corresponds to the linear decay in the log-log graph especially visible for the high energy curve plotted in red. Finally the radiated energy decreases $\propto \exp(-\omega h/\gamma)$ in the last part of the spectrum.

The transition points in between the three regimes are dependent on the impact parameter h and the Lorentz factor γ of the electron. The first inflection point in Fig. 3.3 is only proportional to the inverse of the impact parameter and therefore is the same for each γ. The 1/h dependency can be seen in Fig. 3.4, where the spectrum with $\gamma = 100$ (orange curve from Fig. 3.3) has been plotted for different impact parameters.

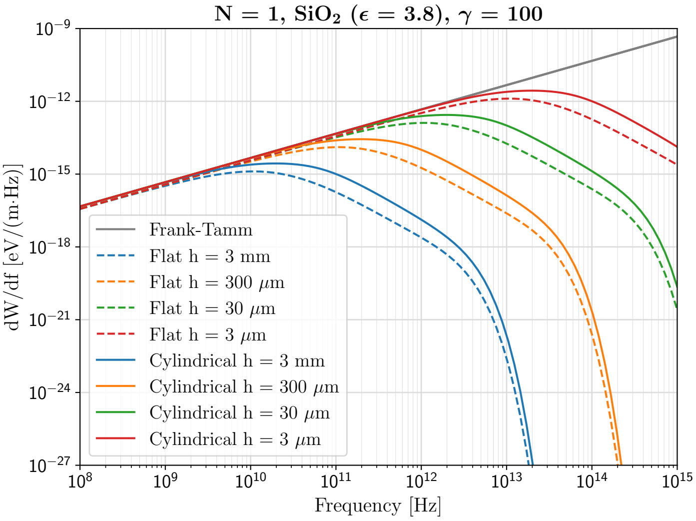

Figure 3.4: Radiated energy spectrum of a single particle for flat and cylindrical geometry for different impact parameters h.

The second turning point of the different spectra shown is proportional to γ/h. The turning point therefore shifts to the right increasing the overall radiated energy with increasing γ as seen in Fig. 3.3, as well as with decreasing the impact parameter h as seen in Fig. 3.4. It is apparent that it shows the same behaviour as the effective radius presented in Eq. (1.1) which can be rewritten as

$$f = \frac{\gamma\, c}{2\pi\, h} \quad \text{with} \quad h = r_{eff}. \tag{3.1}$$

Besides plotting the radiated energy spectra dependent on frequency, it is useful to have a look at the spectra as a function of wavelength as well. Fig. 3.5 shows the

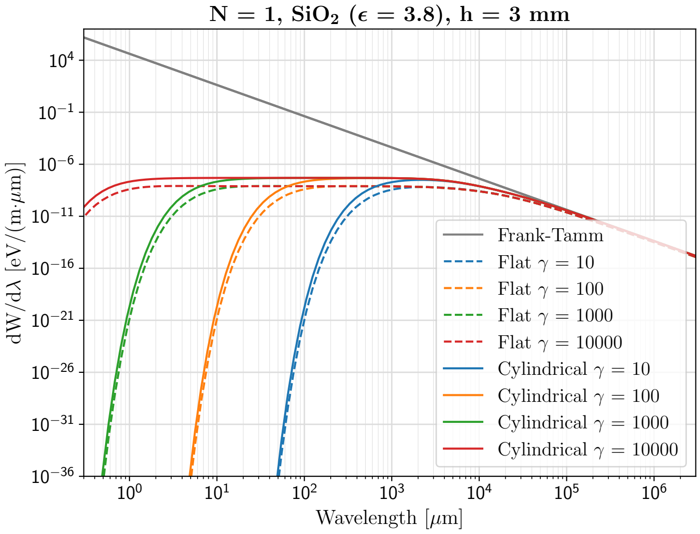

Figure 3.5: Radiated energy spectrum of a single particle for flat and cylindrical geometry for different values of γ.

spectra of Fig. 3.3 as a function of wavelength. Now one can observe the well known $1/\lambda^3$ dependency of Cherenkov radiation. The range $\propto \omega^{-2}$ in the frequency plots transforms to a constant plateau, which can be extended to shorter wavelengths by increasing the energy, or reducing the impact parameter as seen in Figs. 3.5 and 3.6.

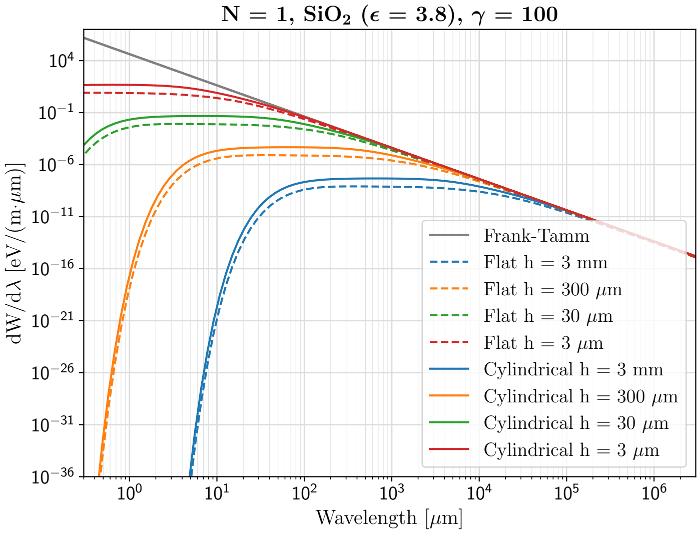

Figure 3.6: Radiated energy spectrum of a single particle for flat and cylindrical geometry for different impact parameters.

3.3 Bunch properties of FCC-ee

As we have just obtained the radiated energy spectrum of a single particle in section 3.2 it is only left to determine the bunch profiles and the number of particles. In Fig. 3.7 typical longitudinal bunch profiles for all four operation modes are presented. The profiles take into account the lengthening effects due to beamstrahlung. The standard deviation σ of a Gaussian fit is given for each profile respectively and presented in Tab. 3.1. As expected the resulting bunch lengths in Tab. 3.1 are in good agreement with [AAA$^+$19, p. 283].

		Z	**WW**	**H(ZH)**	**t$\bar{\text{t}}$**
Bunch length with Beamstrahlung	[ps]	42.2	20.1	17.7	8.4
Bunch length with Beamstrahlung	[mm]	12.7	6.0	5.3	2.5

Table 3.1: Bunch lengths for the different operation modes obtained from Fig. 3.7.

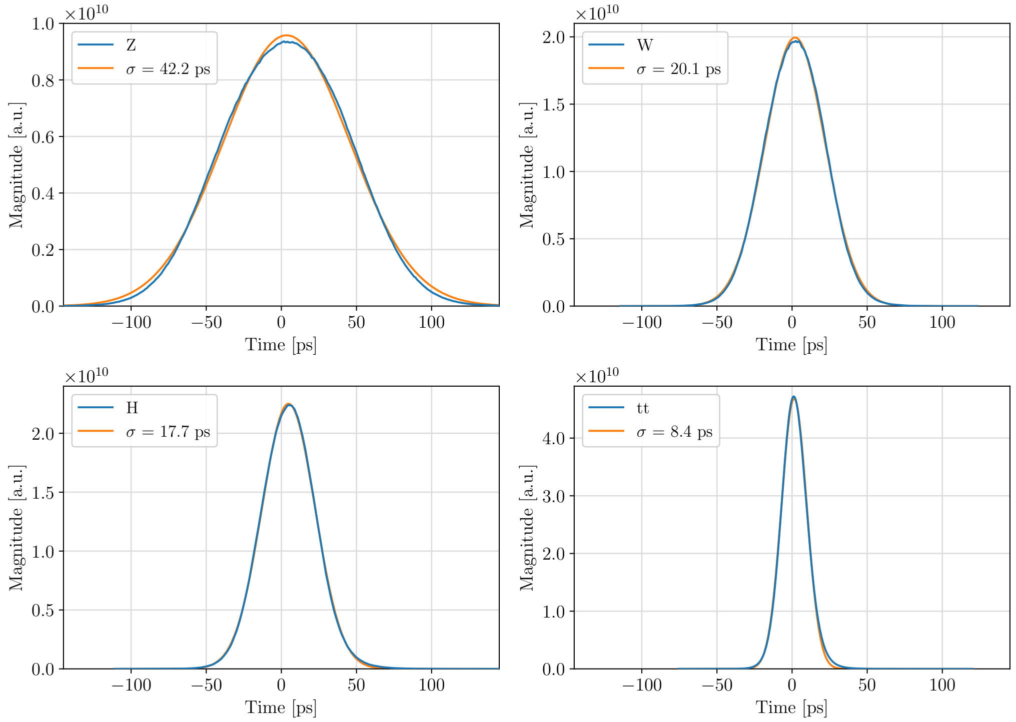

Figure 3.7: Longitudinal bunch profiles [Sha20] for the different operation modes presented in Tab. 1.1. For each profile a Gaussian fit is plotted with the corresponding standard deviation σ shown in the legend. The time scale is the same on each plot, the bunch intensities are unified.

Besides the bunch length (= longitudinal bunch size), we also have a look at the transverse size of the bunch. The minimal and maximal values for the expected transverse sizes have already been presented in Tab. 1.2. There we can see that the transverse beam size in the horizontal plane ranges from 60-150 μm, whereas the transverse beam size in the vertical plane ranges from 10-20 μm.

The three-dimensional bunch form factor which was introduced in Eq. (2.42) is defined as the Fourier transform of the three-dimensional particle density distribution

$$F_{3D}(\vec{k}) = \int S_{3D}(\vec{r})\; e^{-i\vec{k}\vec{r}} d\vec{r}\,.$$

In Fig. 3.8 a 3D schematic of such a particle density distribution is given. In order to illustrate the greatest possible transverse spread with respect to the bunch length, for plotting the particle density distribution the shortest possible bunch length from Fig. 3.7, together with the largest expected transverse sizes are used. This results in a bunch from $\mathrm{t}\bar{\mathrm{t}}$ operation mode with the dimensions $\sigma_z = 2.52$ mm, $\sigma_x = 0.15$ mm and $\sigma_y = 0.02$ mm.

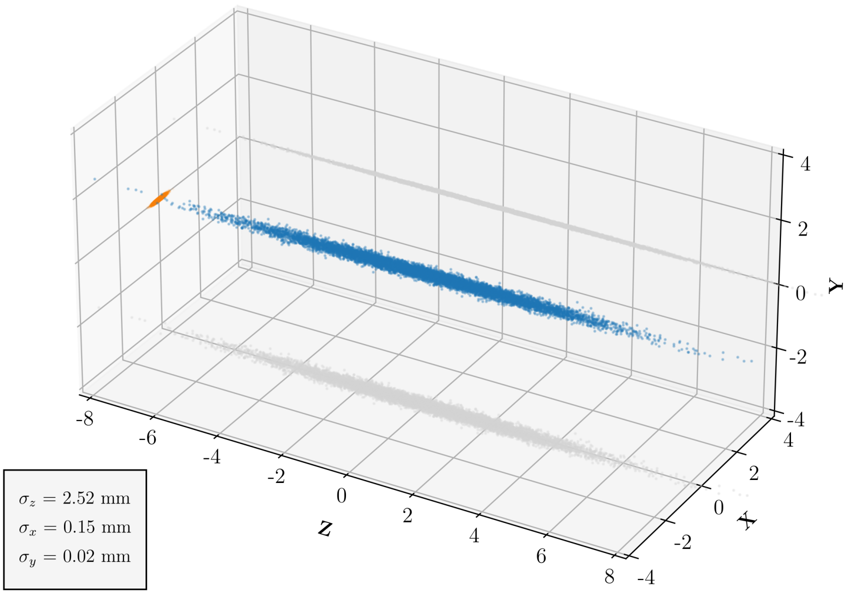

Figure 3.8: 3D schematic of the particle density distribution $S_{3D}(\vec{r})$ during $\mathrm{t}\bar{\mathrm{t}}$ operation.

For all the different operation modes of FCC-ee the longitudinal bunch size is $\approx$ 20-80 times greater than the transverse size in the horizontal plane and $\approx$

120-600 times greater than the transverse size in the vertical plane. The transverse bunch sizes are also small compared to the impact parameters we are interested in. Therefore we neglect the effects of the particles distributed off the center axis and we are left with a particle density distribution in just one dimension. The form factor is then calculated for an infinitely thin bunch.

3.4 Bunch spectra of FCC-ee

The Figs. 3.9 to 3.12 show the radiated energy spectra for the four different operation modes. These plots were created with the cylindrical model, whereas only a fraction of 60° of the full circle is used. The left part of the spectrum from 10^8 Hz up to $\approx 10^{12}$ Hz is dominated by coherent radiation. It is dependent on the form factor of the bunch and extends to higher frequencies for shorter bunches. The coherent spectrum scales with the number of particles in the bunch squared. The second part of the spectrum from $\approx 10^{12}$ Hz up to 10^{15} is the incoherent part. This range only scales linearly with the number of particles in the bunch. The values for each operation mode can also be found in Tab. 1.1.

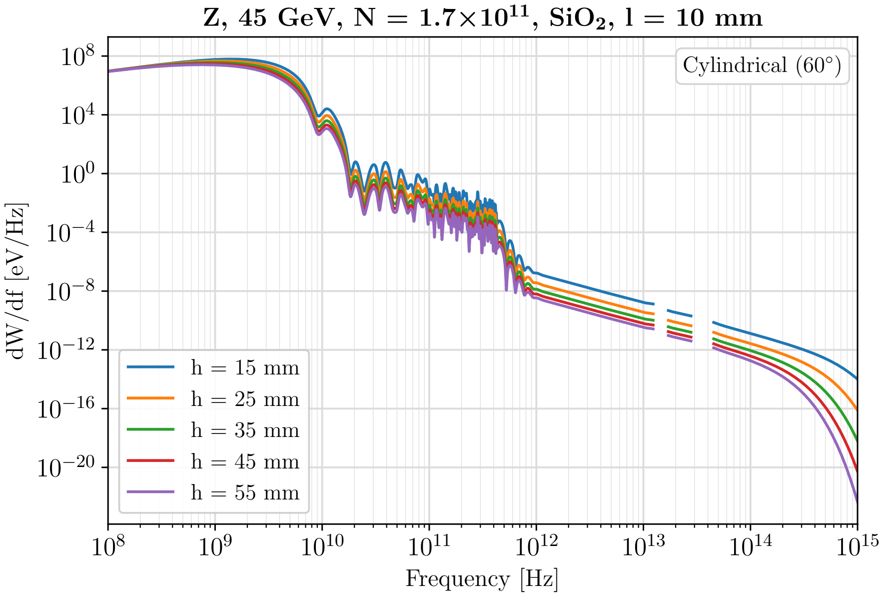

Figure 3.9: Radiated energy spectrum of a 45 GeV electron/positron bunch for different impact parameters. Profile as seen in Fig. 3.7.

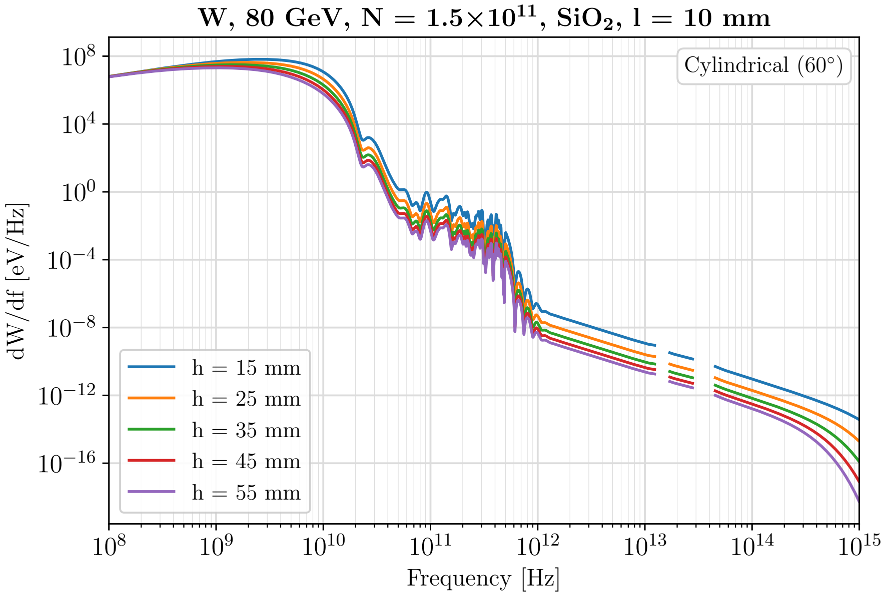

Figure 3.10: Radiated energy spectrum of an 80 GeV electron/positron bunch for different impact parameters. Profile as seen in Fig. 3.7.

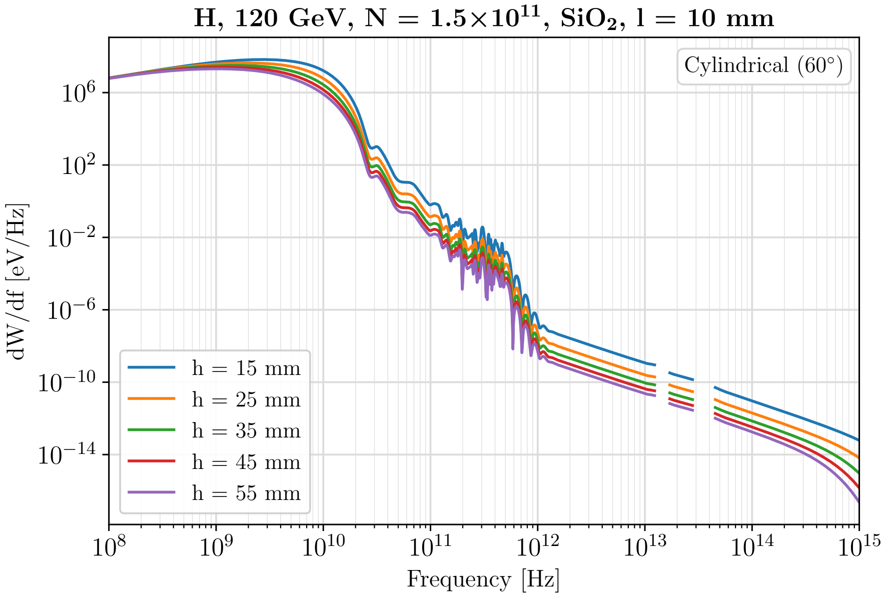

Figure 3.11: Radiated energy spectrum of a 120 GeV electron/positron bunch for different impact parameters. Profile as seen in Fig. 3.7.

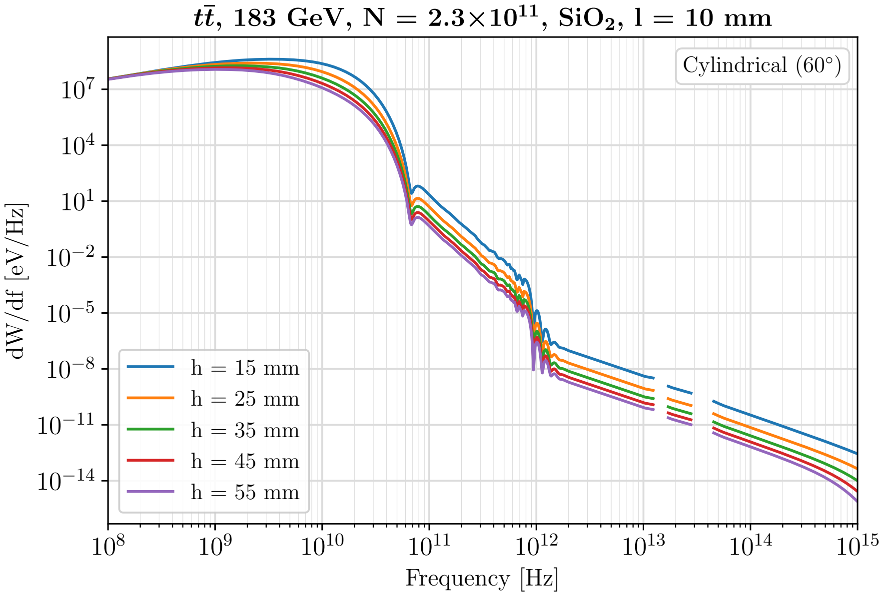

Figure 3.12: Radiated energy spectrum of a 183 GeV electron/positron bunch for different impact parameters. Profile as seen in Fig. 3.7.

3.5 Applications of incoherent radiation

In this section we will have a closer look at the incoherent part of the radiated energy spectra shown in Figs. 3.9 to 3.12. As there is a wide choice of detectors in the visible range (380-780 nm, 789-384 THz) this region is particularly interesting for possible exploitation in beam diagnostics. The following Fig. 3.13 shows the incoherent spectrum for up to 5 μm wavelength. The energy scale is kept the same for better comparison.

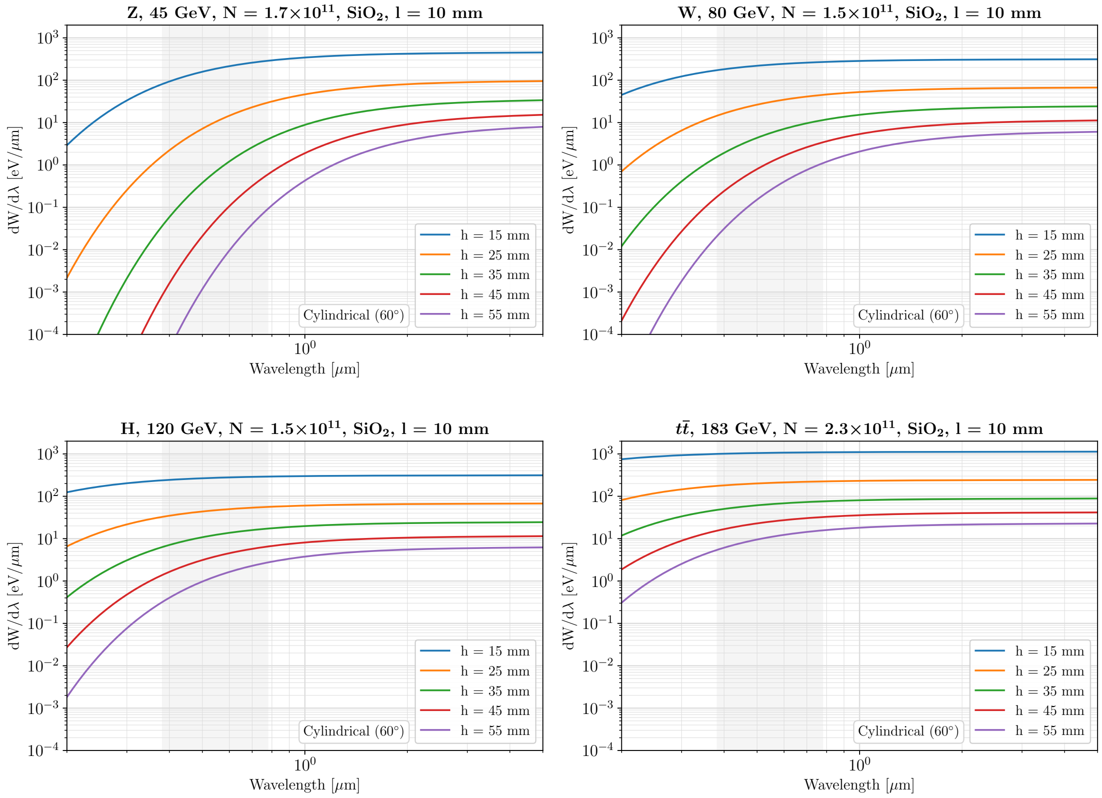

Figure 3.13: Incoherent spectra of the four different bunches. The visible range is slightly emphasised in grey.

Due to the lower particle energy, the exponential decay in the visible range is more prominent for the 45 GeV bunch. For the 183 GeV bunch the region of exponential decay is not so strong as the position of the turning point between the two regimes is $\propto \gamma/h$. For wavelengths longer than ≈ 4 μm all four presented spectra are already saturated in terms of particle energy, meaning their difference in particle energy has no impact on the spectrum. Their difference in radiated energy is just dependent on the number of particles for these wavelengths.

3.5.1 Beam position monitor

Using the different spectra shown in Fig. 3.13 we will now calculate the response of a beam position monitor detecting the emitted photons. To do so we integrate the spectrum over a defined wavelength range to obtain the energy radiated in this range. This integration is done for a grid of 101 impact parameters, linearly distributed from 17.5-52.5 mm. This change in impact parameter corresponds to an offset from -50% to +50% with respect to the central position of 35 mm in the vacuum pipe. Two detectors situated at opposite sides of the beam pipe are considered. Their signals are then plotted as difference over sum (Δ/Σ). This describes the setup for a BPM in one plane. The geometry is shown in Fig. 3.14 for an impact parameter of 35 mm. Adding the same setup rotated by 90° along the vacuum pipe axis would result in a four button BPM as shown in Fig. 1.4.

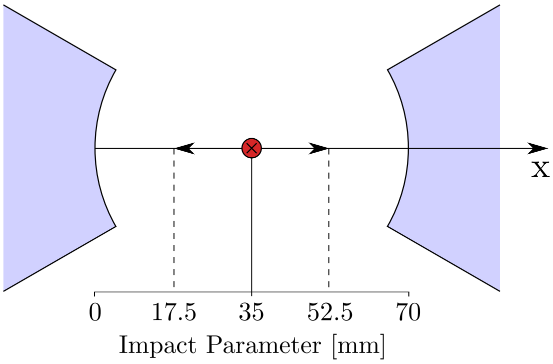

Figure 3.14: Illustration of BPM calculations for an impact parameter of $h = 35$ mm. The impact parameter varies from 17.5-52.5 mm.

Visible spectrum

In Fig. 3.15a the response of a BPM sensitive in the visible spectrum (380-780 nm) is shown for the Z operation mode. Also the curves corresponding to the particle energy changed by ±10% are shown. In Fig. 3.15b the number of photons per detector as a function of impact parameter is shown, whereas the same particle energies as in Fig. 3.15a are considered. For small deviations within a few mm from the central position the signals from the BPM can be characterized by a linear response. The slope of this response at the central position is given as k_0 and is a quantity characterizing the position sensitivity of the BPM. In Fig. 3.15a k_0 is given in values of mm^{-1}. The higher the value the more sensitive the BPM is, however, at the same time this narrows the range in which the BPM can operate without saturating.

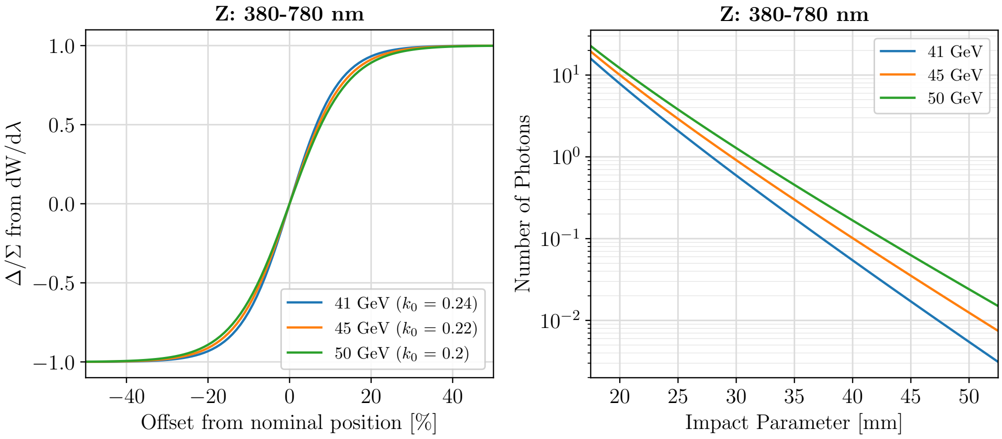

(a) Response of a BPM operated in Δ/Σ mode. (b) Number of photons per detector.

Figure 3.15: BPM response and number of photons for a 45 GeV electron/positron bunch in the visible range (380-780 nm). Nominal particle energy is plotted in orange and a change in particle energy of ±10% is shown as well. $\mathrm{d}W/\mathrm{d}\lambda$ is obtained with parameters given in Fig. 3.13.

The BPM plots and the expected number of photons for the other operation modes are shown in Figs. A.1 to A.4. The first row in these plots corresponds to the visible range from 380-780 nm. Taking the data from these plots in Tab. 3.2 the different values of k_0 for a BPM operating in the visible spectrum are given.

380-780 nm		**h = 35 mm**		
$\boldsymbol{i}$		**90% · γ_i**	**100% · γ_i**	**110% · γ_i**
Z	k_0 [mm^{-1}]	0.238	0.219	0.203
W	k_0 [mm^{-1}]	0.156	0.146	0.138
H	k_0 [mm^{-1}]	0.123	0.117	0.113
t$\bar{\text{t}}$	k_0 [mm^{-1}]	0.104	0.101	0.098

Table 3.2: Overview of the response of a BPM operating in the visible range for the four different operation modes. Values are taken from Figs. A.1 to A.4, γ_i denotes the nominal particle energy at each operation mode respectively.

As can be seen in Tab. 3.2 the BPM is most sensitive for an operation in Z mode. This is expected when comparing to Fig. 3.13 as the Z operation mode has the largest spread in radiated energy for different impact parameters. This larger spread is due to the fact that the 45 GeV bunch has a significantly lower particle energy than the other bunches and therefore does not extend to higher frequencies due to the effective radius of the field (Eq. (3.1)). In this energy regime where the effective radius plays a significant role one is still dependent on the particle energy as can also be seen in Tab. 3.2. For a 10% change in particle energy in Z mode the position sensitivity at $h = 35$ mm changes up to 9%, in $t\bar{t}$ mode about 3%.

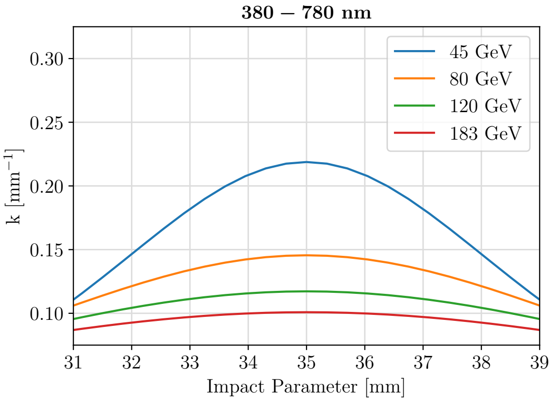

Figure 3.16: Position sensitivity of a BPM in the visible range. The values at the nominal position $k(35\text{ mm}) \coloneqq k_0(35\text{ mm})$ can be found in Tab. 3.2.

380-780 nm		**h = 35 mm**		
$\boldsymbol{i}$		$\mathbf{90\% \cdot \gamma_i}$	$\mathbf{100\% \cdot \gamma_i}$	$\mathbf{110\% \cdot \gamma_i}$
Z	No. of photons/bunch	0.18	0.30	0.45
W	No. of photons/bunch	1.05	1.33	1.60
H	No. of photons/bunch	2.20	2.50	2.76
$\mathbf{t\bar{t}}$	No. of photons/bunch	11.79	12.54	13.14
Z	No. of photons/turn	2939	4980	7568
W	No. of photons/turn	2093	2659	3203
H	No. of photons/turn	865	983	1083
$\mathbf{t\bar{t}}$	No. of photons/turn	566	602	631

Table 3.3: Number of photons in the visible range for an impact parameter of 35 mm. γ_i denotes the nominal particle energy at each operation mode respectively.

Besides the position sensitivity of the BPM the expected number of photons which can be detected is of great importance for an operational device. As can be seen in Fig. 3.15b the number of photons in Z mode spans over more than three orders of magnitude for the presented change in impact parameter. Looking at Fig. 3.13 it is evident that a high position sensitivity comes at the cost of less radiated energy.

This effect is shown in Tab. 3.3. In the visible range the number of photons is more dependent on a change in particle energy for low energy bunches due to the exponential decrease of the radiated energy. For a 10% change in particle energy in Z mode the number of photons at $h = 35$ mm changes at least by 40%, in $\mathrm{t\bar{t}}$ mode at least 5%. In general at an impact parameter of $h = 35$ mm the photon yield in the visible range is not high enough for a bunch-by-bunch measurement, providing turn-by-turn data would be feasible.

Another possibility to increase the photon yield would be to reduce the impact parameter as shown in Tab. 3.4. This would also increase position sensitivity as seen in Tab. 3.5. Moreover, the number of photons is not as dependent on a change in particle energy anymore. For a 10% change in particle energy the change in number of photons at $h = 5$ mm is less than 3% for all operation modes.

	380-780 nm		**h = 15 mm**	
i		**90%** $\cdot\, \gamma_i$	**100%** $\cdot\, \gamma_i$	**110%** $\cdot\, \gamma_i$
Z	No. of photons/bunch	33.48	39.20	44.27
W	No. of photons/bunch	42.15	44.72	46.76
H	No. of photons/bunch	50.29	51.71	52.80
$\mathbf{t\bar{t}}$	No. of photons/bunch	197.19	199.65	201.50
	380-780 nm		**h = 5 mm**	
i		**90%** $\cdot\, \gamma_i$	**100%** $\cdot\, \gamma_i$	**110%** $\cdot\, \gamma_i$
Z	No. of photons/bunch	2038	2084	2119
W	No. of photons/bunch	1518	1529	1537
H	No. of photons/bunch	1551	1556	1559
$\mathbf{t\bar{t}}$	No. of photons/bunch	5645	5652	5658

Table 3.4: Number of photons/bunch in the visible range for impact parameters of 15 mm and 5 mm. γ_i denotes the nominal particle energy at each operation mode respectively.

380-780 nm

$\boldsymbol{i}$		**35 mm**	**15 mm**	**5 mm**
Z	$k_0\,[\mathrm{mm}^{-1}]$	0.219	0.292	0.638
W	$k_0\,[\mathrm{mm}^{-1}]$	0.146	0.234	0.612
H	$k_0\,[\mathrm{mm}^{-1}]$	0.117	0.216	0.605
$\mathbf{t\bar{t}}$	$k_0\,[\mathrm{mm}^{-1}]$	0.101	0.207	0.602

Table 3.5: Overview of the response of a BPM operating in the visible range for the four different operation modes and different impact parameters. The nominal particle energy γ_i is used for each case respectively.

Visible spectrum with bandpass filters

After the full visible range we now want to have a closer look at specific wavelengths in the visible range. For this a bandpass filter in the blue (470 ± 10 nm) as well as in the red (670 ± 10 nm) were chosen. The BPM graphs and the expected number of photons for all four operation modes are shown in Figs. A.1 to A.4. Just as for the full visible range we present on overview of the position sensitivity in Tab. 3.6.

470 ± 10 nm **h = 35 mm**

$\boldsymbol{i}$		**90%** $\cdot\,\boldsymbol{\gamma_i}$	**100%** $\cdot\,\boldsymbol{\gamma_i}$	**110%** $\cdot\,\boldsymbol{\gamma_i}$
Z	$k_0\,[\mathrm{mm}^{-1}]$	0.340	0.307	0.281
W	$k_0\,[\mathrm{mm}^{-1}]$	0.199	0.182	0.169
H	$k_0\,[\mathrm{mm}^{-1}]$	0.145	0.135	0.127
$\mathbf{t\bar{t}}$	$k_0\,[\mathrm{mm}^{-1}]$	0.114	0.109	0.105

670 ± 10 nm **h = 35 mm**

$\boldsymbol{i}$		**90%** $\cdot\,\boldsymbol{\gamma_i}$	**100%** $\cdot\,\boldsymbol{\gamma_i}$	**110%** $\cdot\,\boldsymbol{\gamma_i}$
Z	$k_0\,[\mathrm{mm}^{-1}]$	0.243	0.221	0.203
W	$k_0\,[\mathrm{mm}^{-1}]$	0.150	0.139	0.131
H	$k_0\,[\mathrm{mm}^{-1}]$	0.117	0.112	0.107
$\mathbf{t\bar{t}}$	$k_0\,[\mathrm{mm}^{-1}]$	0.100	0.097	0.095

Table 3.6: Overview of the response of a BPM with blue (470 ± 10 nm) or red (670 ± 10 nm) bandpass filter for the four different operation modes. Values are taken from Figs. A.1 to A.4, γ_i denotes the nominal particle energy at each operation mode respectively.

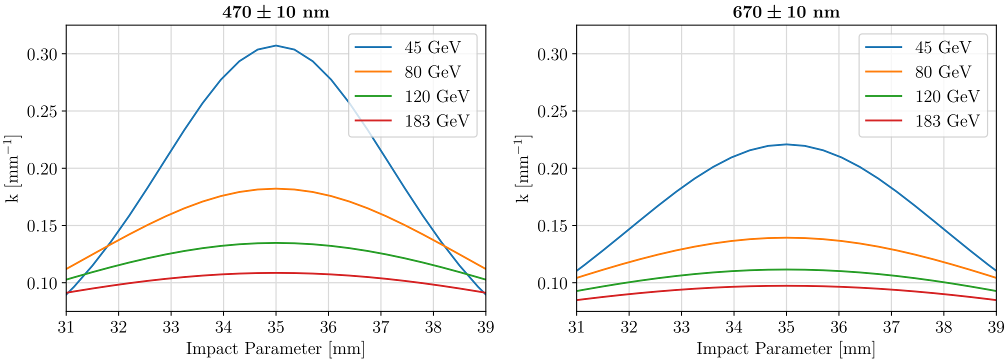

Figure 3.17: Position sensitivity of BPMs with blue (470 ± 10 nm) or red (670 ± 10 nm) bandpass filter. The values at the nominal position $k(35 \text{ mm}) := k_0(35 \text{ mm})$ can be found in Tab. 3.6.

We can see that the position sensitivity is highest for short wavelengths at low beam energies. When changing the filter from red to blue in Z mode the position sensitivity increases by about 39%, in $\mathrm{t\bar{t}}$ mode about 12%. As already mentioned this increase of position sensitivity goes hand in hand with a decrease in detectable photons, as can be seen in Tabs. 3.7 and 3.8. When changing the filter from red to blue and operating with nominal particle energy in Z mode the number of photons reduces by about 92%, with nominal particle energy in $\mathrm{t\bar{t}}$ mode the reduction is about 43%. This drastic decrease suggests that also the position sensitivity in the full visible range is highly dominated by the lower energy part of the spectrum. This can easily be validated when comparing Tab. 3.2 with Tab. 3.6.

As expected from the previous section the number of detectable photons per bunch will be small with narrow bandpass filters. The photon yield per bunch given in Tabs. 3.7 and 3.8 for an impact parameter of $h = 35$ mm can be increased by reducing the impact parameter. This behaviour is shown in Tab. 3.9.

470 ± 10 nm **h = 35 mm**

i		**90% · γ_i**	**100% · γ_i**	**110% · γ_i**
Z	No. of photons/bunch	7.56 e−04	1.82 e−03	3.66 e−03
W	No. of photons/bunch	1.84 e−02	2.72 e−02	3.66 e−02
H	No. of photons/bunch	6.07 e−02	7.41 e−02	8.62 e−02
$\mathbf{t\bar{t}}$	No. of photons/bunch	4.04 e−01	4.43 e−01	4.76 e−01
Z	No. of photons/turn	12.6	30.3	60.9
W	No. of photons/turn	36.8	54.4	73.2
H	No. of photons/turn	23.9	29.1	33.9
$\mathbf{t\bar{t}}$	No. of photons/turn	19.4	21.3	22.8

Table 3.7: Number of photons with a bandpass filter at 470 nm for an impact parameter of 35 mm. γ_i denotes the nominal particle energy at each operation mode respectively.

670 ± 10 nm **h = 35 mm**

i		**90% · γ_i**	**100% · γ_i**	**110% · γ_i**
Z	No. of photons/bunch	1.34 e−02	2.31 e−02	3.52 e−02
W	No. of photons/bunch	7.75 e−02	9.64 e−02	1.13 e−01
H	No. of photons/bunch	1.49 e−01	1.65 e−01	1.79 e−01
$\mathbf{t\bar{t}}$	No. of photons/bunch	7.41 e−01	7.77 e−01	8.06 e−01
Z	No. of photons/turn	223.0	384.4	585.7
W	No. of photons/turn	155.0	192.8	226.0
H	No. of photons/turn	58.6	64.8	70.3
$\mathbf{t\bar{t}}$	No. of photons/turn	35.6	37.3	38.7

Table 3.8: Number of photons with a bandpass filter at 670 nm for an impact parameter of 35 mm. γ_i denotes the nominal particle energy at each operation mode respectively.

470 ± 10 nm

i		**35 mm**	**15 mm**	**5 mm**
Z	No. of photons/bunch	1.82 e−03	1.06 e+00	8.07 e+01
W	No. of photons/bunch	2.72 e−02	1.59 e+00	6.11 e+01
H	No. of photons/bunch	7.41 e−02	1.98 e+00	6.27 e+01
$\mathbf{t\bar{t}}$	No. of photons/bunch	4.43 e−01	7.89 e+00	2.28 e+02

670 ± 10 nm

i		**35 mm**	**15 mm**	**5 mm**
Z	No. of photons/bunch	2.31 e−02	2.68 e+00	1.24 e+02
W	No. of photons/bunch	9.64 e−02	2.77 e+00	8.91 e+01
H	No. of photons/bunch	1.65 e−01	3.09 e+00	9.02 e+01
$\mathbf{t\bar{t}}$	No. of photons/bunch	7.77 e−01	1.17 e+01	3.27 e+02

Table 3.9: Number of photons/bunch with blue (470 ± 10 nm) or red (670 ± 10 nm) bandpass filter and impact parameters of 35 mm, 15 mm and 5 mm. The nominal particle energy γ_i is used for each case respectively.

3.5.2 Longitudinal bunch profile

As we have seen in section 1.2 to estimate the energy spread in the bunches a narrow longitudinal resolution of the bunch profiles shown in Fig. 3.7 is required. A sub-picosecond resolution is necessary, which is at least two orders of magnitudes smaller than a typical bunch length in FCC-ee. To achieve such a narrow gating is a technical challenge on itself, however, time-to-digital conversion methods with tens of fs have already been proposed [CAH06].

In Tab. 3.9 we have just seen that for decreasing the impact parameter the photon yield significantly increases. This effect could possibly be exploited in streak camera measurements. Taking into account a narrow bandwidth of ±10 nm the number of photons is already in the order of $\approx$ 100 photons per bunch for a bandpass filter at 670 nm. Increasing the bandwidth would allow for a further increase in photon yield. This could be a promising approach as a sub-ps resolution with streak cameras has already been demonstrated [WBB$^+$06].

We also want to investigate the feasibility of an approach similar to the longitudinal density monitor (LDM) implemented at LHC [JAB$^+$12], even though the required resolution for FCC-ee is much smaller than the 50 ps resolution achieved with the mentioned LDM. In the following paragraphs we want to investigate the expected photon yield which would result from such a narrow gating.

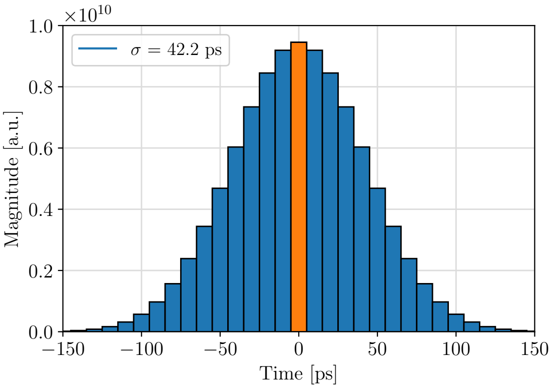

Figure 3.18: Schematic of a longitudinal bunch profile measurement (cf. Fig. 3.7). For illustrative reasons a time frame of 10 ps is shown. So the center column shown in orange is 100 times narrower for the presented calculations.

Due to the narrow time frame the already low numbers of photons per bunch in Tabs. 3.3, 3.7 and 3.8 are reduced even more. It is evident that for such a fine resolution we therefore need to integrate over several turns to accumulate a decent signal. In our estimation the bunch is divided into time frames of 100 fs, turn by turn we accumulate the signal in each of this time frames. Like that we create a histogram of our longitudinal bunch profile and the longer the integration time the higher our dynamic range within each bunch will be.

To estimate the number of photons to expect for the given time frames we calculate the values for the center bar of our histogram for each bunch mode as a reference point. To do so we approximate the different longitudinal bunch profiles by a Gaussian. Their standard deviations are given in Tab. 3.1. First we normalize the distributions to the number of photons obtained at nominal particle energy presented in Tabs. 3.3, 3.7 and 3.8 for an impact parameter of $h = 35$ mm. From this distributions we consider a time frame of 100 fs centered around the maximum of the Gaussian. This provides us with an estimation of the maximal number of photons per bunch to expect within the given time frame.

Now it is only left with the number of turns, as we want to accumulate the signal of a single bunch over several turns. With a circumference of 97.756 km each bunch yields ≈ 3066.74 turns per second. As the longitudinal single bunch profiles can be obtained within several minutes, the values in Tab. 3.10 are provided for an integration time of 1 minute. In the same way these calculations then have been performed for an impact parameter of $h = 15$ mm and $h = 5$ mm.

At $h = 35$ mm the expected number of photons is small especially for the low energy bunches. It is about three orders of magnitude smaller than for the high energy bunches. The smaller the impact parameter the smaller this gap between the bunches gets, reducing to about one order of magnitude for $h = 5$ mm. At such a small impact parameter even a narrow bandpass filter at a short wavelength (470 ± 10 nm) leads to a significant photon yield in the order of at least 10^4 for all the bunch modes.

As a time frame of 100 fs is small compared to the typical bunch length in FCC-ee, the values given in Tab. 3.10 can be used to estimate the number of photons per bunch and minute at a different point in time. Since the values in Tab. 3.10 correspond to the peak of a Gaussian, dividing this value by $\sqrt{e}$ yields the number of photons at an offset in time of $1\sigma_i$. Note that the standard deviation σ_i is different for each operation mode.

$\boldsymbol{i}$		**within 100 fs**		
	470 ± 10 nm	**35 mm**	**15 mm**	**5 mm**
Z	Max. photons/(bunch · minute)	3.17 e−01	1.84 e+02	1.40 e+04
W	Max. photons/(bunch · minute)	9.93 e+00	5.81 e+02	2.23 e+04
H	Max. photons/(bunch · minute)	3.08 e+01	8.21 e+02	2.60 e+04
$\mathbf{t\bar{t}}$	Max. photons/(bunch · minute)	3.88 e+02	6.90 e+03	2.00 e+05
	670 ± 10 nm	**35 mm**	**15 mm**	**5 mm**
Z	Max. photons/(bunch · minute)	4.02 e+00	4.65 e+02	2.15 e+04
W	Max. photons/(bunch · minute)	3.52 e+01	1.01 e+03	3.25 e+04
H	Max. photons/(bunch · minute)	6.88 e+01	1.28 e+03	3.74 e+04
$\mathbf{t\bar{t}}$	Max. photons/(bunch · minute)	6.80 e+02	1.02 e+04	2.86 e+05
	380-780 nm	**35 mm**	**15 mm**	**5 mm**
Z	Max. photons/(bunch · minute)	5.21 e+01	6.82 e+03	3.63 e+05
W	Max. photons/(bunch · minute)	4.85 e+02	1.63 e+04	5.58 e+05
H	Max. photons/(bunch · minute)	1.04 e+03	2.14 e+04	6.45 e+05
$\mathbf{t\bar{t}}$	Max. photons/(bunch · minute)	1.10 e+04	1.74 e+05	4.94 e+06

Table 3.10: Maximal number of photons per bunch and minute within a time frame of 100 fs for different wavelength ranges. The nominal particle energy γ_i is used for each case respectively. The photon yield is given for three different impact parameters.

3.6 Applications of coherent radiation

In this section we will have a closer look at the coherent part of the radiated energy spectra shown in Figs. 3.9 to 3.12. The following Fig. 3.19 shows the coherent spectrum in the frequency range from 1 GHz to 200 GHz. Note that for better comparability to the previous section in this section the length of the radiator l is still considered to be 10 mm even though $\lambda < l$ does not hold for frequencies < 30 GHz. In real applications this would lead to a low frequency cut-off of the radiated energy spectrum. However, the results presented can easily be linearly scaled to any desired radiator length.

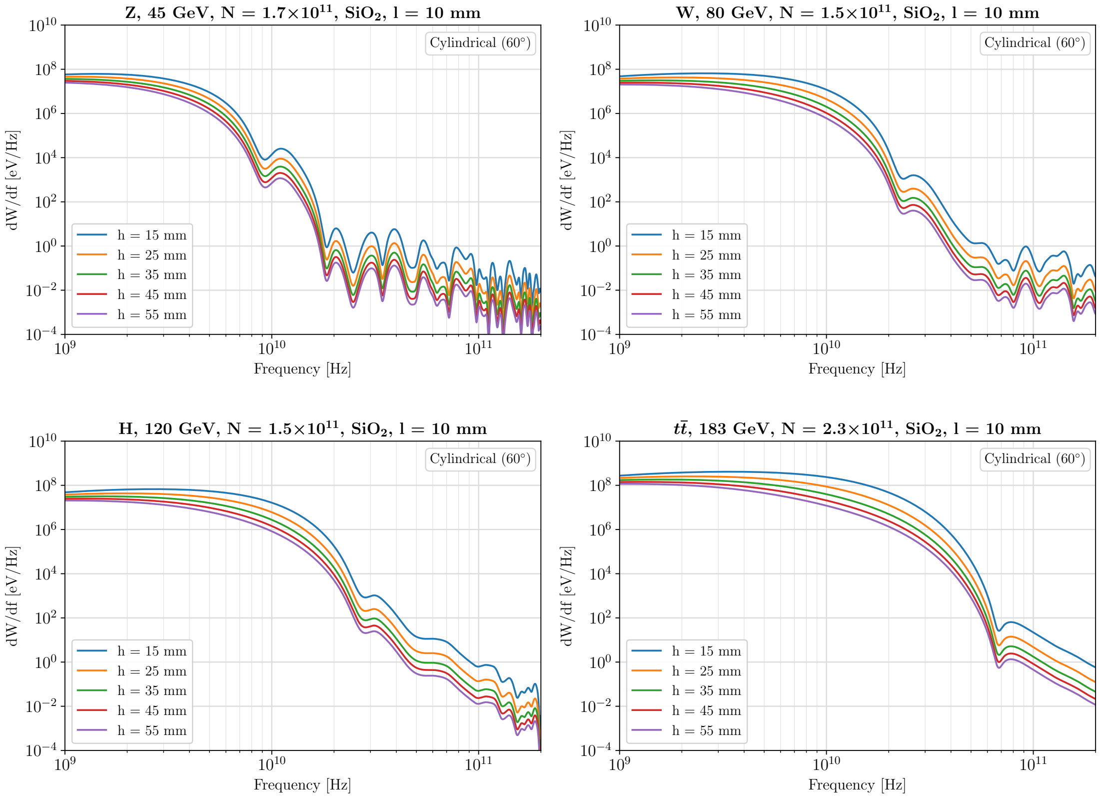

Figure 3.19: Coherent part of the radiated energy spectra for the four different bunches.

In contrast to the incoherent part of the spectra shown in Fig. 3.13 the lower energy of the 45 GeV bunch compared to the other bunch modes is not leading to a decrease in radiated energy. In this frequency range all four bunch modes already saturate the spectrum in terms of particle energy. This can be seen on the very left of the plots at 1 GHz where the radiated energy only changes because of the different number of particles in each bunch. The reason for the differences in radiated energy is linked to the different bunch lengths. The shorter the bunch the higher frequencies contribute to the coherent spectrum. Looking at the spectra in Fig. 3.19 each shows a rather smooth decline from left to right before increasing slightly again. Up to this first inflection point the spectra are dominated by their Gaussian approximation which is given by their different standard deviations σ_i. The deviation from the Gaussian shape dominates the spectra for frequencies higher than the mentioned inflection point and corresponds to the higher frequency components of the bunch profiles.

3.6.1 Beam position monitor

Using the different spectra shown in Fig. 3.19 we will now calculate the response of a beam position monitor detecting the emitted photons. Just as described in section 3.5.1 we integrate the spectrum over a defined frequency range to obtain the energy radiated in this range. Again we use a grid of 101 impact parameters, linearly distributed from 17.5-52.5 mm. This change in impact parameter corresponds to an offset from -50% to +50% with respect to the central position of 35 mm in the vacuum pipe. So the geometry is again as shown in Fig. 3.14.

In Fig. 3.20a the response of a BPM operating with a bandpass filter at 25 ± 1 GHz is shown for the Z operation mode. Also the curves for a change of ±10% in particle energy are shown. As already mentioned the change in particle energy does not effect this part of the spectrum. In Fig. 3.20b the number of photons per detector as a function of impact parameter is shown. For small deviations within several mm from the central position the signals from the BPM can be characterized by a linear response. The slope of this response at the central position is given as k_0 and is a quantity for the position sensitivity of the BPM. In Fig. 3.20a k_0 is given in values of mm^{-1}.

The BPM plots and the expected number of photons for the other operation modes are shown in Figs. A.5 to A.8. The first row in these plots corresponds to a bandpass filter of 5 ± 0.2 GHz, the second row to 25 ± 1 GHz and the third row to 100 ± 4 GHz. Taking the data from these plots in Tab. 3.11 the different values of k_0 for a BPM operating at different frequencies are shown.

As can be seen in Tab. 3.11 the BPM has the same position sensitivity for the different bunch modes. Looking at Fig. 3.19 this is expected, as the spectra are independent of the different bunch energies and the difference in number of particles cancels out in the Δ/Σ plots. However, the position sensitivity changes for different bandpass filters. As we have seen in section 3.2 the spectrum approaches the Frank-Tamm behaviour for low frequencies with wavelengths longer or comparable to the impact parameter. A wavelength of 35 mm corresponds to a frequency of

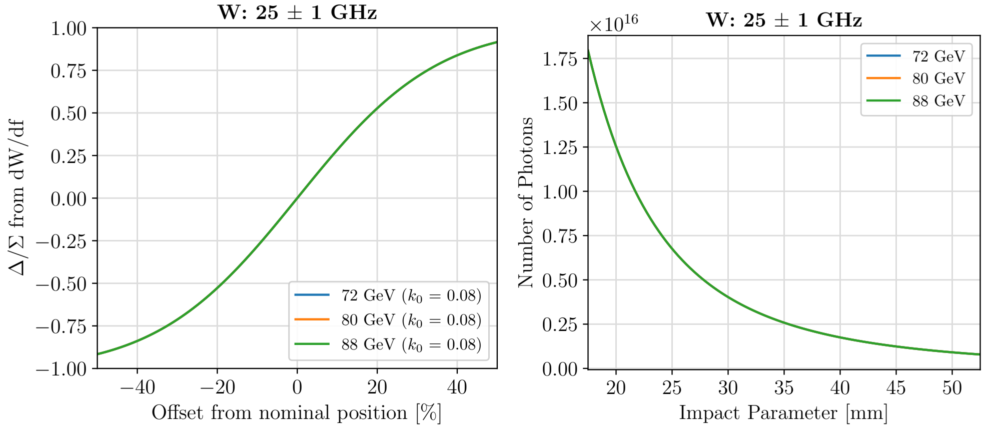

(a) Response of a BPM operated in Δ/Σ mode.
(b) Number of photons per detector.

Figure 3.20: BPM response and number of photons for an 80 GeV electron/positron bunch at 25 GHz. A change in particle energy is negligible. dW/df is obtained with parameters given in Fig. 3.19.

		5 GHz	**25 GHz**	**100 GHz**
Z/W/H/t$\bar{\text{t}}$	k_0 [mm^{-1}]	0.052	0.083	0.086

Table 3.11: Overview of the response of a BPM in the coherent range for the four different operation modes. Values are taken from Figs. A.5 to A.8. The position sensitivity is much lower in the coherent part of the spectrum than in the incoherent part (cf. Tab. 3.2).

≈ 8.6 GHz. A bandpass filter below this frequency will therefore show a different behaviour than a bandpass filter above this frequency. This also can be seen in the different regimes of the spectrum of the single particle introduced in section 3.2. So for $\lambda \gg h$ we do not expect any change in the spectra and therefore $k_0 = 0$. For f < 8.6 GHz we expect k_0 to approach 0 and for f > 8.6 GHz we expect k_0 to increase. This behaviour can be seen in Tab. 3.11 as well as in Fig. 3.21.

After studying the position sensitivity of the BPM we now want to investigate the expected number of photons which can be detected. As can be seen in Fig. 3.20b the number of photons in W mode is in the order of 10^{16} using a bandpass filter of 25 GHz. Comparing this to the 1.33 photons at nominal particle energy in the visible spectrum (Tab. 3.3) illustrates the great difference in photon yield between coherent and incoherent radiation. The figures for the other operation modes are shown in Figs. A.5 to A.8 and the expected number of photons at nominal impact

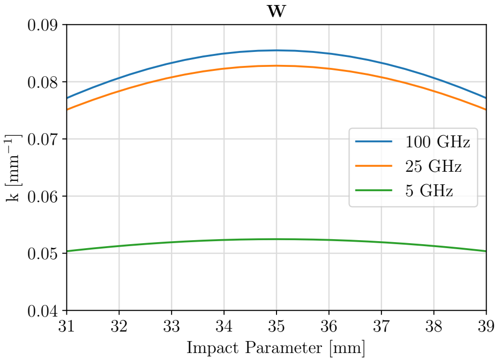

Figure 3.21: Position sensitivity of a BPM for an 80 GeV electron/positron bunch with bandpass filters in the coherent part of the spectrum. The values at the nominal position $k(35\text{ mm}) \coloneqq k_0(35\text{ mm})$ can be found in Tab. 3.11.

parameter of 35 mm are summarized in Tab. 3.12.

		γ_i (h = 35 mm)		
i		**5 GHz**	**25 GHz**	**100 GHz**
Z	No. of photons/bunch	5.10 e+19	1.74 e+11	7.83 e+10
W	No. of photons/bunch	2.85 e+20	2.58 e+15	4.29 e+11
H	No. of photons/bunch	3.09 e+20	7.97 e+15	1.00 e+12
$\mathbf{t\bar{t}}$	No. of photons/bunch	2.21 e+21	3.42 e+19	3.42 e+13

Table 3.12: Number of photons/bunch with different bandpass filters for an impact parameter of 35 mm. γ_i denotes the nominal particle energy at each operation mode respectively.

3.6.2 Bunch length monitor

As we have seen in section 1.3 bunch length measurements using Cherenkov diffraction radiation have already been performed successfully at CERN. By measuring the radiated energy spectrum of a bunch at different frequencies the bunch shape can be reconstructed and its bunch length obtained. In this section we want to discuss this approach for the different operation modes at FCC-ee.

In Fig. 3.22 the radiated energy spectra for the four different longitudinal bunch profiles are shown. For frequencies smaller than 1 GHz we observe that the different spectra are very similar to each other expect for a scaling which is due to the different number of particles within the bunches. This similar behaviour has two reasons. First nearly all particles within the bunch radiate coherently for frequencies lower than 1 GHz and moreover we are in a regime of the radiated energy spectrum which is independent from bunch energies within the given range. This is in line with our observation in section 3.2 where we saw that for $f \approx 0.1\, c/h = 0.857$ GHz the spectra approached the Frank-Tamm behaviour. So for frequencies at around 1 GHz we are at a transition regime dependent on the impact parameter.

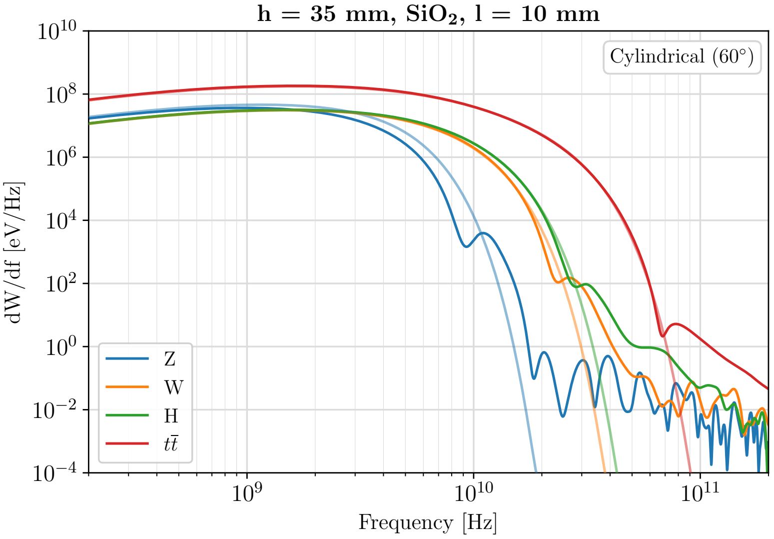

Figure 3.22: Coherent radiated energy spectra of the longitudinal bunch profiles shown in Fig. 3.7. For each FCC-ee bunch spectrum also the spectrum of the Gaussian bunch profile is shown. The standard deviations of the Gaussian distribution are taken from Tab. 3.1.

To introduce an analytical approach for the bunch length calculations we want to restrict ourselves to a regime where the spectrum has an obvious dependency with respect to frequency. For frequencies higher than $f_{II} \approx c/h$ we leave the mentioned transition regime between the first and the second part of the spectrum. For these higher frequencies we are now dominated by the second part of the spectrum as presented in section 3.2 which is $\propto \omega^{-2}$. With an impact parameter of 35 mm this condition corresponds to $f_{II} \approx 8.57$ GHz.

As we now have chosen a lower bound for frequency measurements we are left with the higher bound. In Fig. 3.23 we can see a close-up of the previous figure. The dotted grey line indicates the identified frequency f_{II}. As we want to estimate the bunch length with the help of the standard deviation of a Gaussian distribution in Fig. 3.23 we need to compare the actual FCC-ee spectra (solid dark curve) with the one of the Gaussian estimate (solid light curve). The dotted lines in orange, green and red indicate the position of the first inflection point of the actual spectra. They are located at ≈ 23.5 GHz (W), ≈ 28 GHz (H) and ≈ 68 GHz ($t\bar{t}$). Up to these frequencies the actual spectra show a behaviour as expected from a Gaussian bunch. The Z operation mode is excluded from this analysis as the length of the Z profile is in a similar order of magnitude as the given impact parameter. It would be needed to extend the diameter of the vacuum pipe to fit a larger radiator to measure at lower frequencies. Moreover, during Z operation mode the longitudinal bunch profile deviates more from a Gaussian distribution than the other bunch profiles as can be seen in Fig. 3.7.

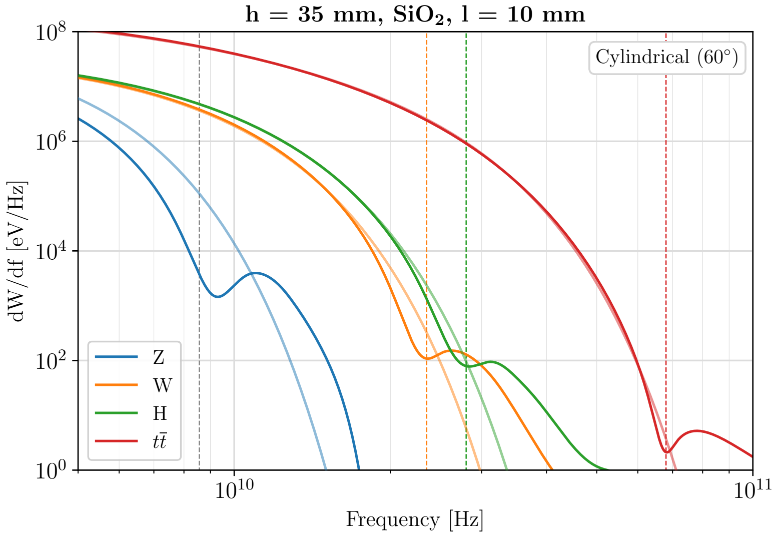

Figure 3.23: Close-up of the coherent spectra in Fig. 3.22. The dotted grey line indicates the start of the second regime of the single particle spectrum at $f_{II} \approx 8.57$ GHz.

As the frequencies we obtained for the W, H and $t\bar{t}$ operation modes are within the range of the spectrum which is still $\propto \omega^{-2}$ we can provide an analytical estimation of the bunch length. Following the same approach as in section 1.3 (see in detail [CBC+20]) we can estimate the bunch length exploiting the knowledge of the radiated energy spectrum of a single particle. We obtain a standard deviation of the bunch of

$$\sigma \approx \sqrt{\left| \frac{1}{\omega_1^2 - \omega_2^2} \cdot \log\left(\frac{S_1\,\omega_1^2}{S_2\,\omega_2^2} \right) \right|} \tag{3.2}$$

whereas S_1 and S_2 correspond to the measured power at the angular frequencies ω_1 and ω_2. Comparing this equation with [CBC+20, Eq. 12] shows that Eq. (3.2) is independent from impact parameter h and particle energy γ. This is due to the fact that we operate in a regime of the spectrum where the impact parameter h has the same influence on both signals and therefore the impact parameter h cancels out in the relation between S_1 and S_2. On top of that for the frequency ranges obtained above the radiated energy spectra of a single particle do not change within the given energy scales.

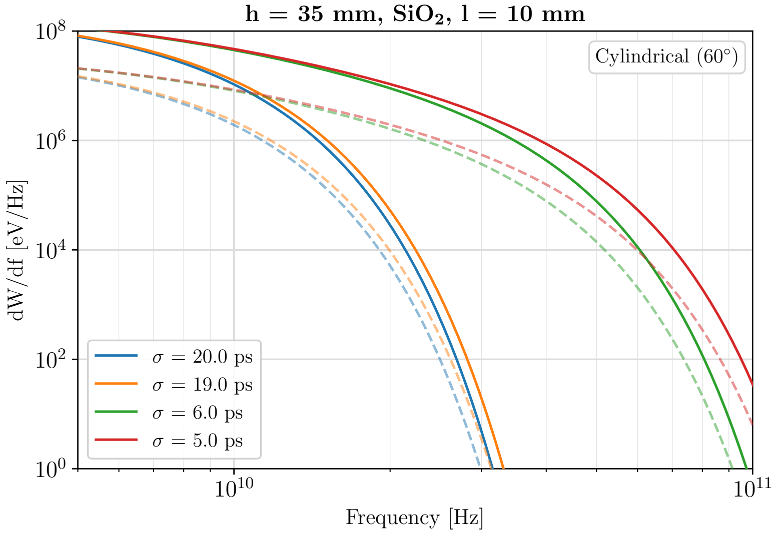

Figure 3.24: Close-up of coherent radiated energy spectra for bunch lengths with 1 ps difference. The dashed line indicates the smallest number of particles (1.5×10^{11}), the solid line the highest number of particles (2.3×10^{11}) in FCC-ee operation modes.

So with measuring the power at only two frequencies a Gaussian bunch profile can be estimated. Next we want to investigate how the radiated energy spectra change for different bunch parameters. In Fig. 3.24 a change in σ of 1 ps is shown for the shortest and longest bunches in FCC-ee (except Z operation mode). The solid lines refer to the maximal number of particles in a bunch, the dashed lines refer to the smallest number of particles.

In Tab. 3.13 the changes in signal for a change in bunch length of 1 ps at different frequencies are given for the two limiting cases of 20 and 6 ps. It is evident that for a higher sensibility of a change in bunch length, the measurement frequency should increase the shorter the bunches to be measured. The difference in number of particles has no effect on the data provided in Tab. 3.13, however, for the given values the radiated energy increases by a factor of ≈ 5.5 when the number of particles is increased.

In Fig. 3.24 one can also observe that a high dynamic range of the detector is needed if one wants to measure the bunch length from 20 to 5 ps with the help of only two frequencies. Whereas at 10 GHz the signal increases by a factor of ≈ 4.4, at 25 GHz the signal increases by four order of magnitudes when the bunch length changes from 20 to 5 ps. To achieve a higher bunch length sensitivity over the full range of bunch lengths and at the same time avoid the need of a high dynamic range detector it would be useful to use different detectors at several frequencies ranging from 10 to 50 GHz. On top of that more frequencies would allow for a more precise profile measurement including derivations from a Gaussian shape. For this Eq. (3.2) would need to be replaced and calculated numerically.

		h = 35 mm		
bunch length		**10 GHz**	**25 GHz**	**50 GHz**
from 20 to 19 ps	Increase in signal [%]	16.7	162.1	4.8 e−3
from 6 to 5 ps	Increase in signal [%]	4.5	31.3	196.6

Table 3.13: Signal sensibility for a change in bunch length at different frequencies at an impact parameter of 35 mm. The value at 50 GHz for the 19 ps long bunch is negligible, as the bunch length is not short enough to have a decent contribution to the coherent spectrum at this frequency.

4

Conclusion and outlook

Simulations of Cherenkov diffraction radiation (ChDR) for dielectric beam diagnostic devices have been performed in the framework of FCC-ee. The calculations for the radiated energy spectrum of a single particle are valuable for benchmarking other simulation models of ChDR, which contain different use cases of ChDR. E.g. models which include several layers of material [L^{+}20, Mou12] or real-life sizes of radiators [H^{+}20, KMP^{+}18]. The infinite dimensions of the flat and the cylindrical models introduced allow the determination of an upper bound of the radiated energy due to ChDR. Possible future improvements of the calculations performed include more realistic geometries and the consideration of other sources of radiation, e.g. diffraction radiation.

We have seen that the high particle energies, in FCC-ee would allow for applications of incoherent radiation even at large impact parameters. For high position sensitivity BPMs the detected wavelengths should be as small as possible while still providing a large enough photon yield. A decrease in impact parameter or a measurement accumulated over many bunches can be performed to provide enough photons. Especially for high particle energies and large impact parameters the advantage of higher position sensitivity in the visible range (Tab. 3.2) becomes negligible in comparison to high measurement frequencies of the coherent spectrum (Tab. 3.11).

To perform longitudinal bunch profile measurements on a bunch-by-bunch basis similar as done at LHC [JAB^{+}12] the nominal impact parameter at FCC-ee of 35 mm would have to be reduced to achieve a sufficient photon yield as seen in Tab. 3.10. The narrow time resolution of 100 fs may be achieved with streak cameras where sub-ps resolution has been demonstrated [WBB^{+}06].

In contrast to the incoherent part of the spectra, the coherent part of the spectra provides a vast number of photons even at impact parameters of 35 mm (Tab. 3.12). This leads to a smaller position resolution, whereas higher flux of photons allows for bunch-by-bunch spectrum measurements. Moreover, electro-optic techniques may facilitate the use of coherent ChDR to achieve the intended bunch profile resolution [FBB$^+$19, S$^+$18]. However, considering that the absolute time resolution of the produced coherent ChDR needs to be measured. Also, bunch length measurements are feasible during W, H, and $\mathrm{t\bar{t}}$ operation mode, whereas for the Z operation mode an adaption of the vacuum pipe to allow for larger radiators may be required. As the position sensitivity would be very similar for the frequencies needed for the bunch length measurement, information on both beam position and bunch length may be extracted from a single non-invasive measurement.

For actual testing in the incoherent spectrum, one would require the highest energy particles available, which naturally will be below FCC-ee particle energies. To compensate for the lower particle energies and still be able to reproduce the FCC-ee spectral behaviour the impact parameter can be decreased to achieve a comparable spectrum as seen in Figs. 3.4 and 3.6. Possible electron accelerators for research in the incoherent spectrum include the SuperKEKB at KEK (High Energy Accelerator Research Organisation) in Japan (7.0 GeV) [AFK18], the Diamond Light Source at Harwell Science and Innovation Campus in Oxfordshire in England (3.0 GeV) [Dia19] and the Karlsruhe Research Accelerator (KARA) at KIT (Karlsruhe Institute of Technology) in Germany (2.5 GeV) [PBB$^+$18].

For further investigations, the requirements for the coherent part of the radiated energy spectrum of a particle bunch are easier to be met in terms of energy. We have seen in Fig. 3.3 that the low-frequency part of the spectrum does not change even at low particle energies. This is the case for frequencies lower than in Eq. (3.1). Beam position and bunch length studies in the coherent spectrum therefore can also be performed at lower energy research accelerators like CLEAR at CERN in Switzerland (200 MeV) [G$^+$18].

APPENDIX A

BPM data

A.1 Incoherent radiation

Figs. A.1 to A.4 are using the parameters given at Fig. 3.13. The common ones are

– Dielectric material:	SiO_2
– Radiator length l:	10 mm
– Geometry:	Cylindrical (60°)

A.2 Coherent radiation

Figs. A.5 to A.8 are using the parameters given at Fig. 3.19. The common ones are

– Dielectric material:	SiO_2
– Radiator length l:	10 mm
– Geometry:	Cylindrical (60°)

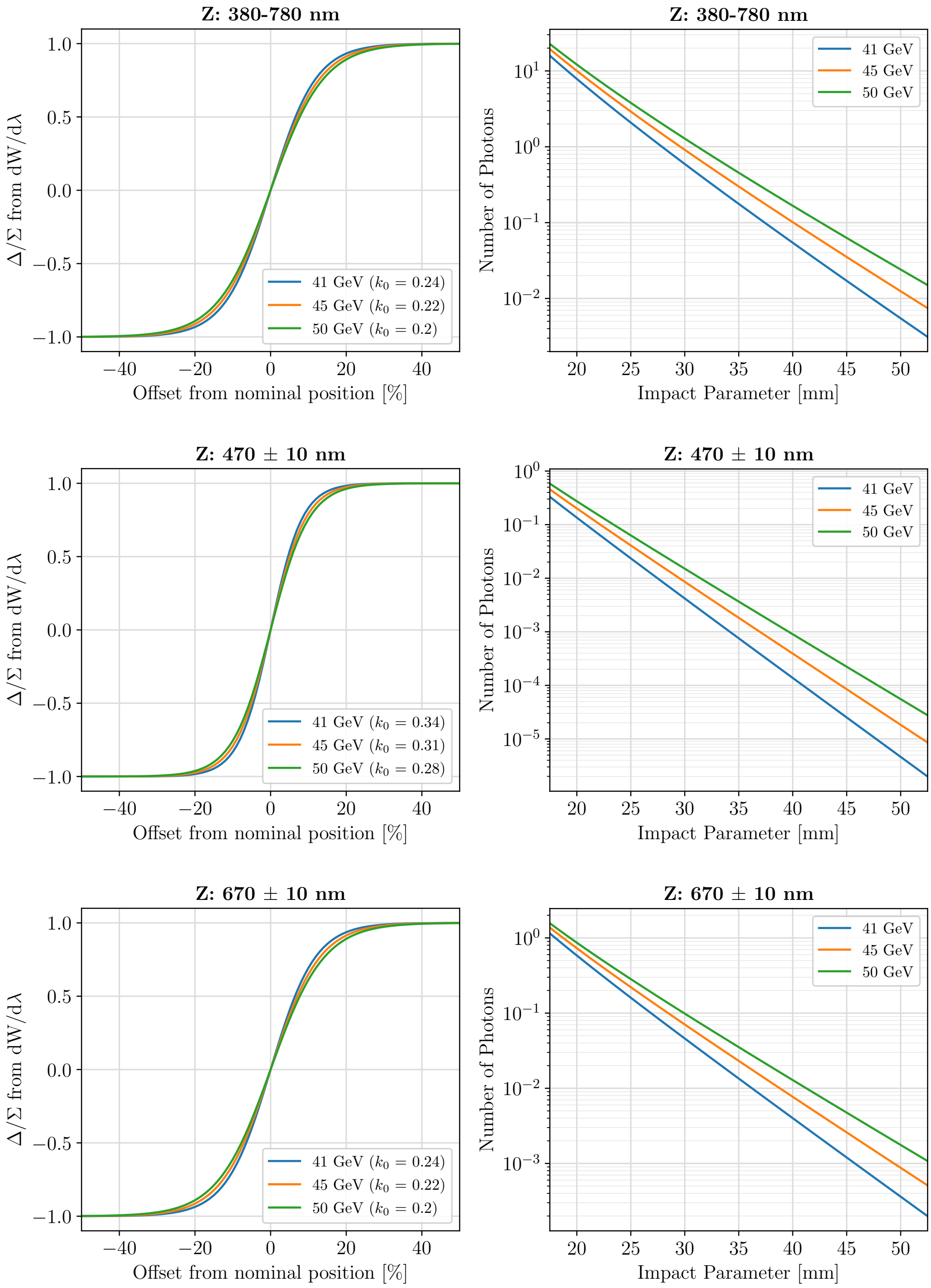

Figure A.1: Δ/Σ and number of photons for a 45 GeV electron/positron bunch. First row shows the full visible range (380-780 nm), second row shows filtering in the blue (470 nm) and third row shows filtering in the red (670 nm).

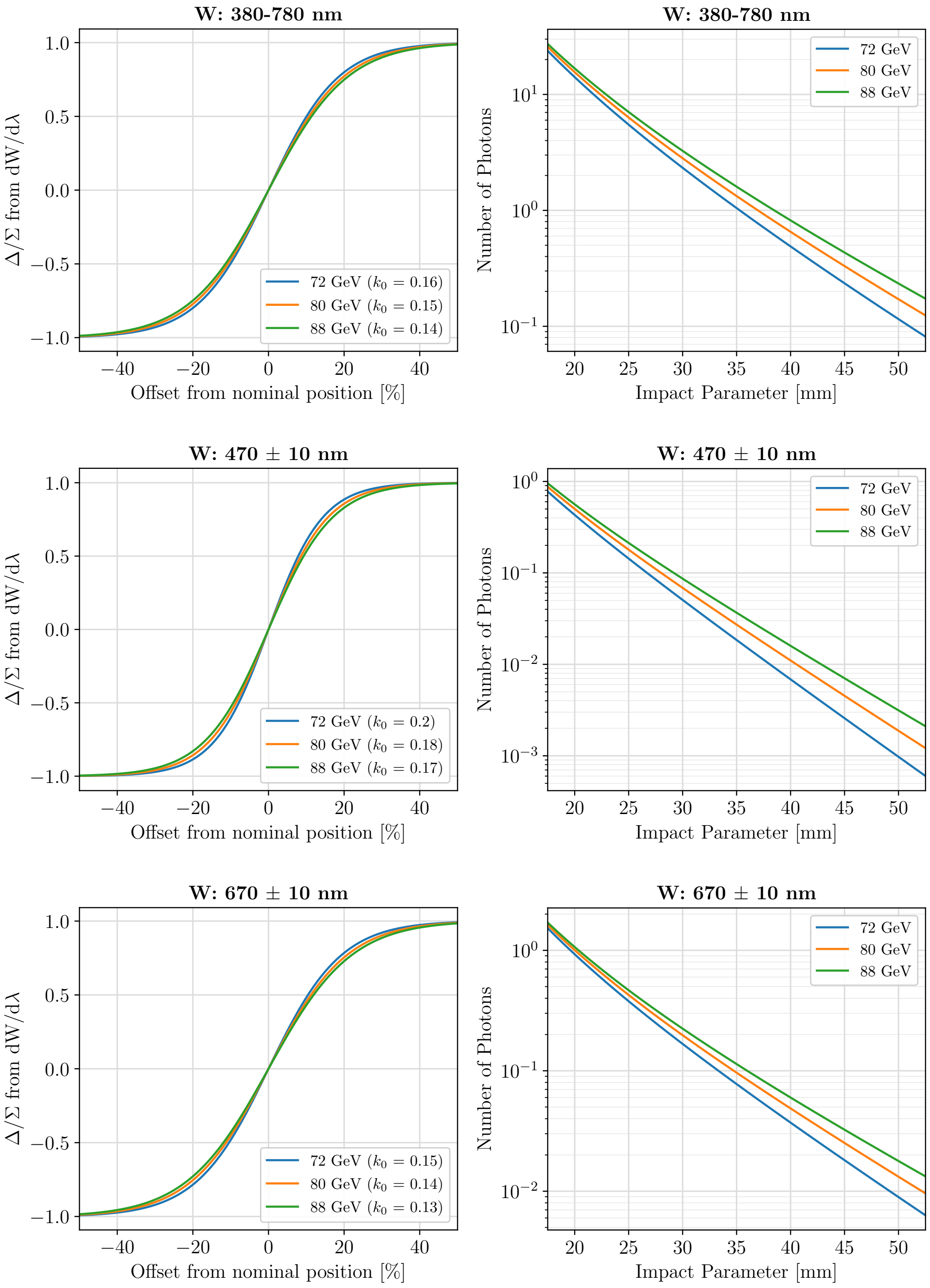

Figure A.2: Δ/Σ and number of photons for an 80 GeV electron/positron bunch. First row shows the full visible range (380-780 nm), second row shows filtering in the blue (470 nm) and third row shows filtering in the red (670 nm).

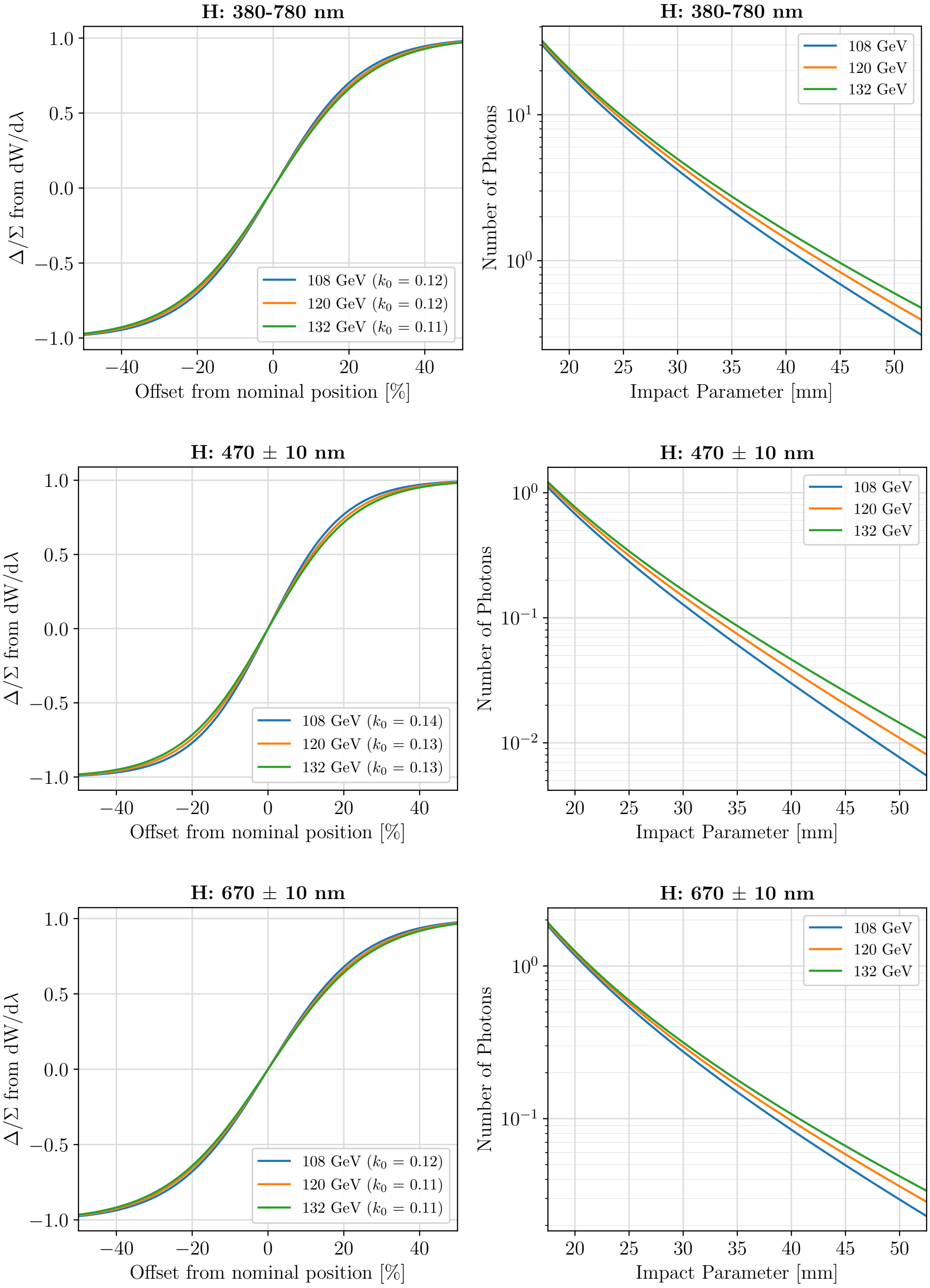

Figure A.3: Δ/Σ and number of photons for a 120 GeV electron/positron bunch. First row shows the full visible range (380-780 nm), second row shows filtering in the blue (470 nm) and third row shows filtering in the red (670 nm).

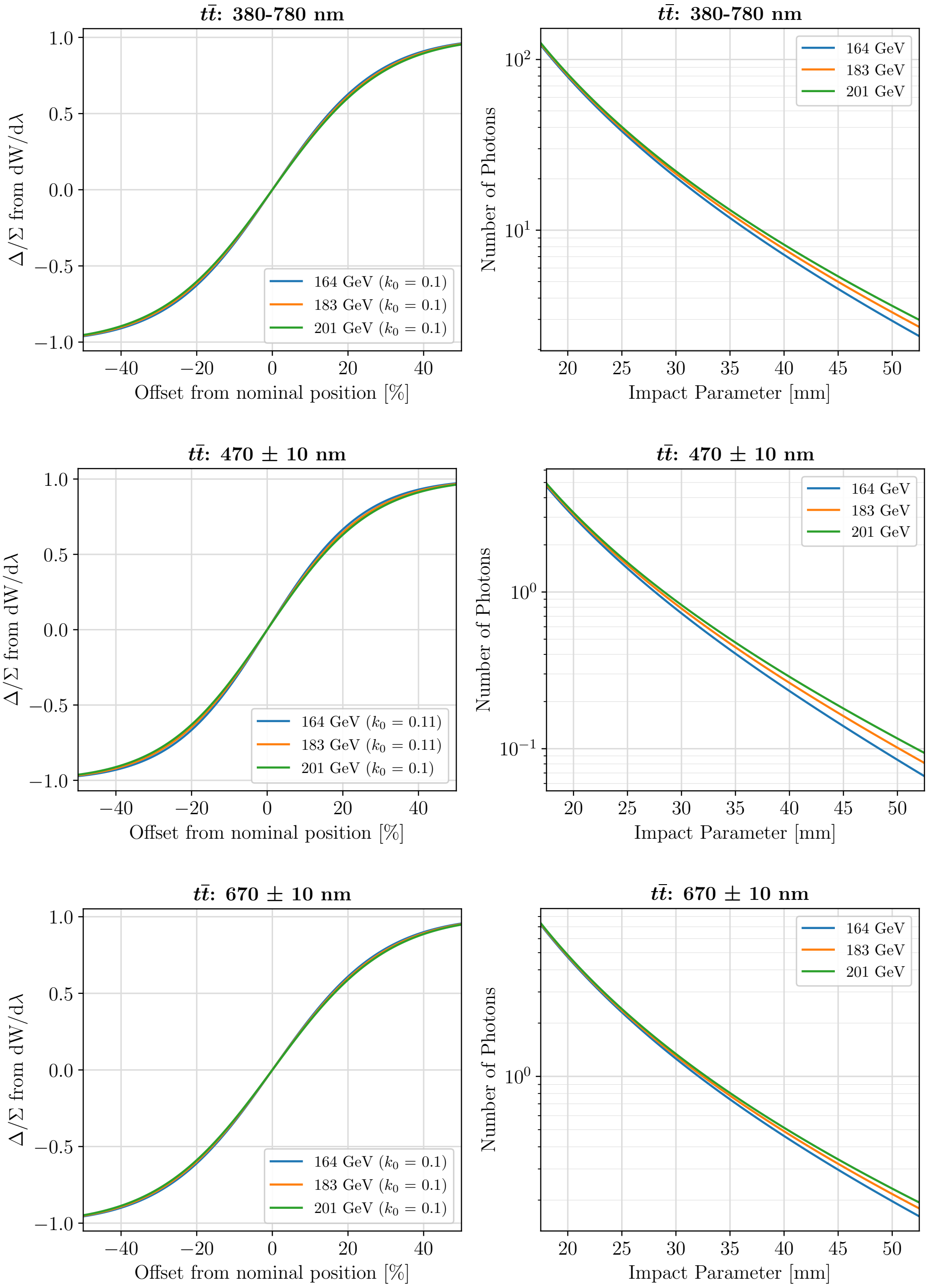

Figure A.4: Δ/Σ and number of photons for a 183 GeV electron/positron bunch. First row shows the full visible range (380-780 nm), second row shows filtering in the blue (470 nm) and third row shows filtering in the red (670 nm).

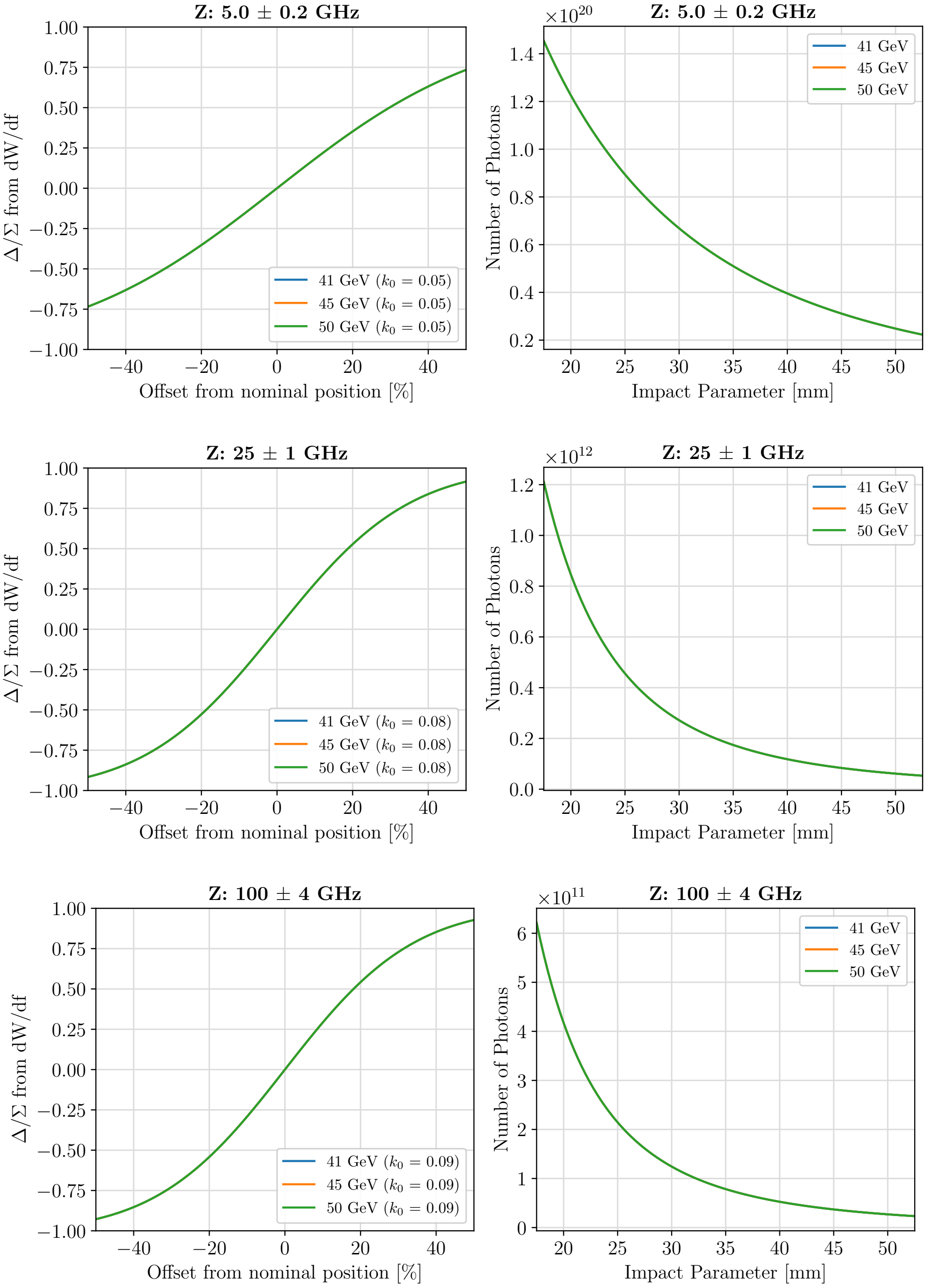

Figure A.5: Δ/Σ and number of photons for a 45 GeV electron/positron bunch. First row shows band pass filter centered at 5 GHz, second row at 25 GHz and third row at 100 GHz.

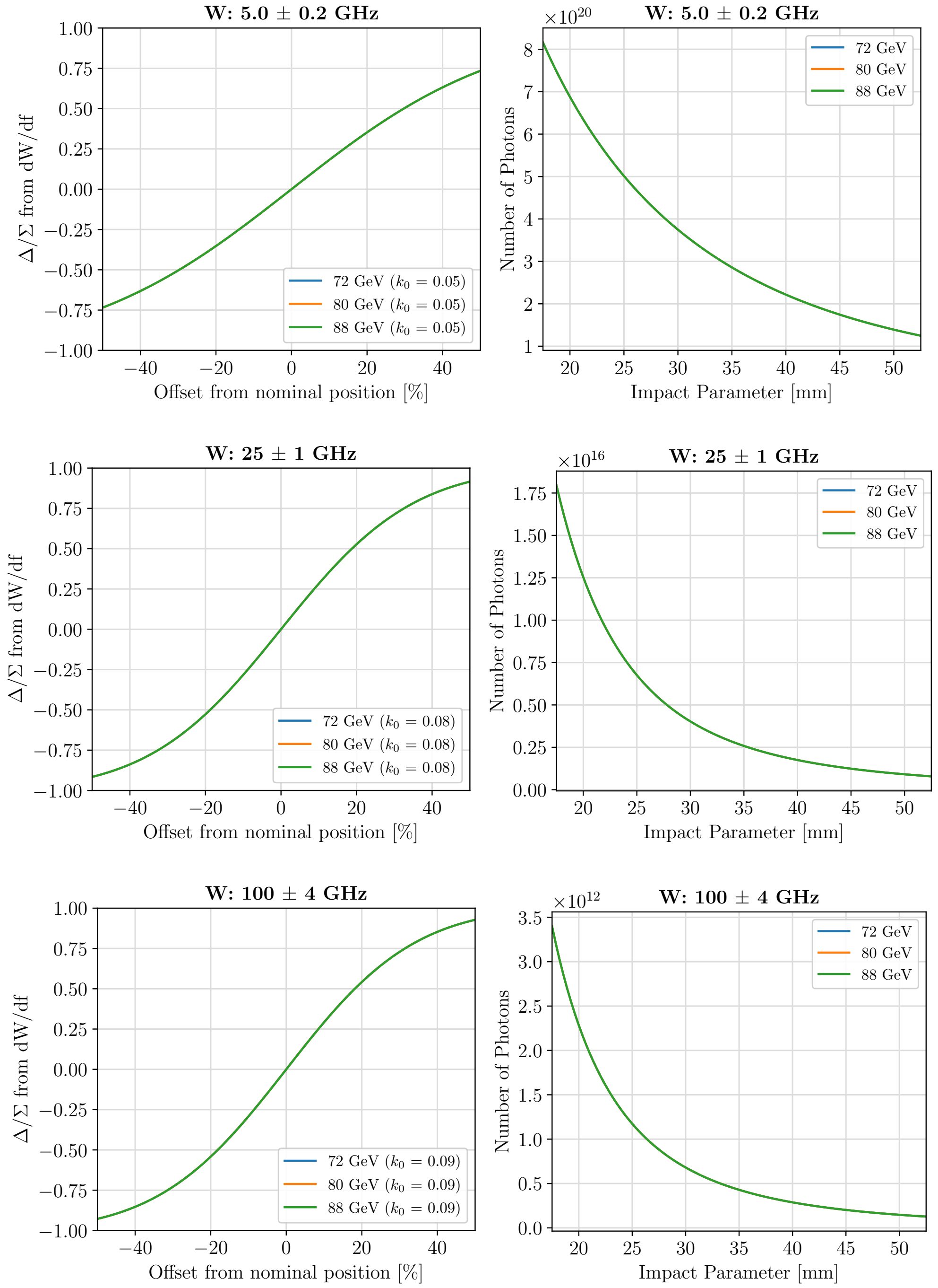

Figure A.6: Δ/Σ and number of photons for an 80 GeV electron/positron bunch. First row shows band pass filter centered at 5 GHz, second row at 25 GHz and third row at 100 GHz.

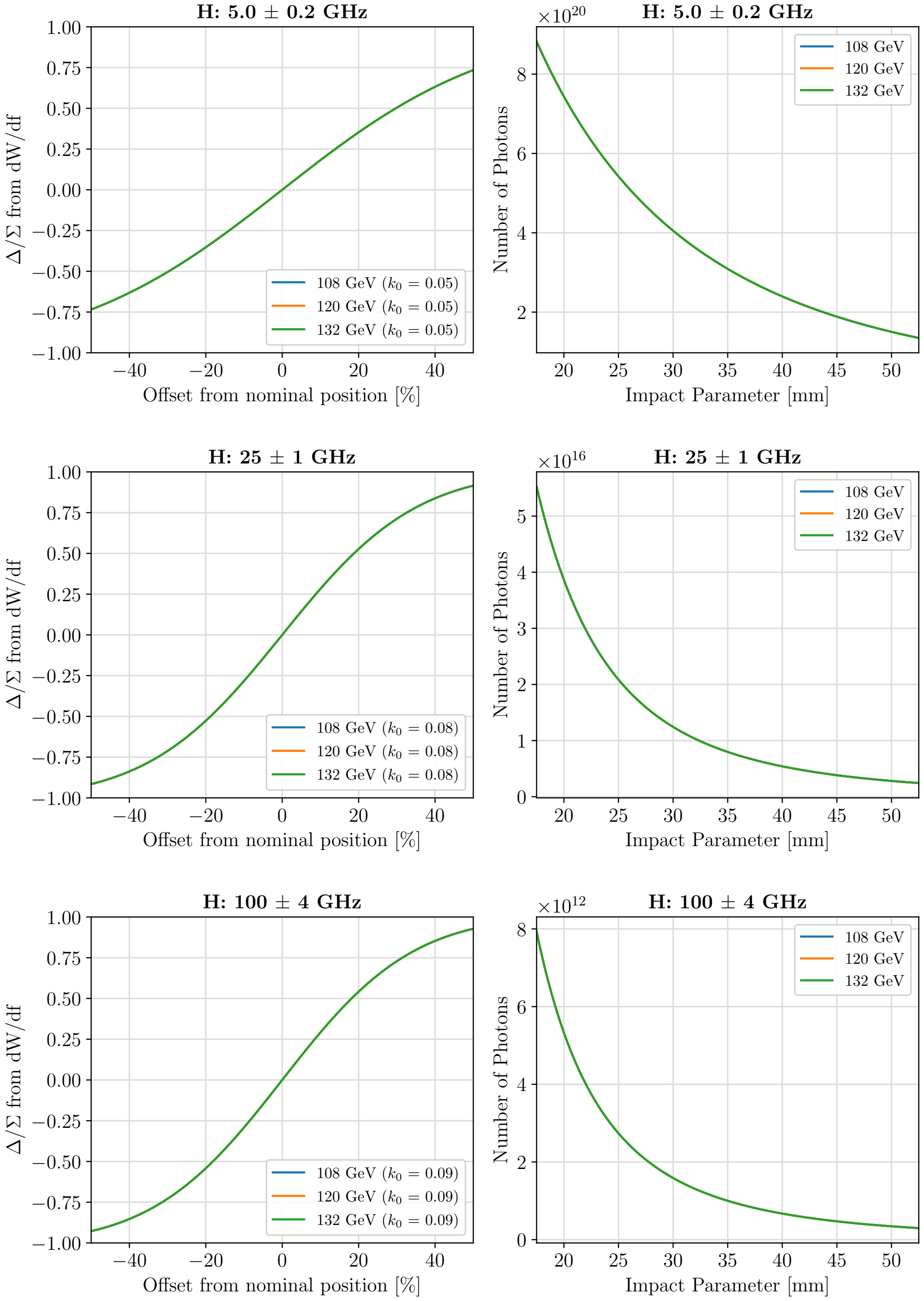

Figure A.7: Δ/Σ and number of photons for a 120 GeV electron/positron bunch. First row shows band pass filter centered at 5 GHz, second row at 25 GHz and third row at 100 GHz.

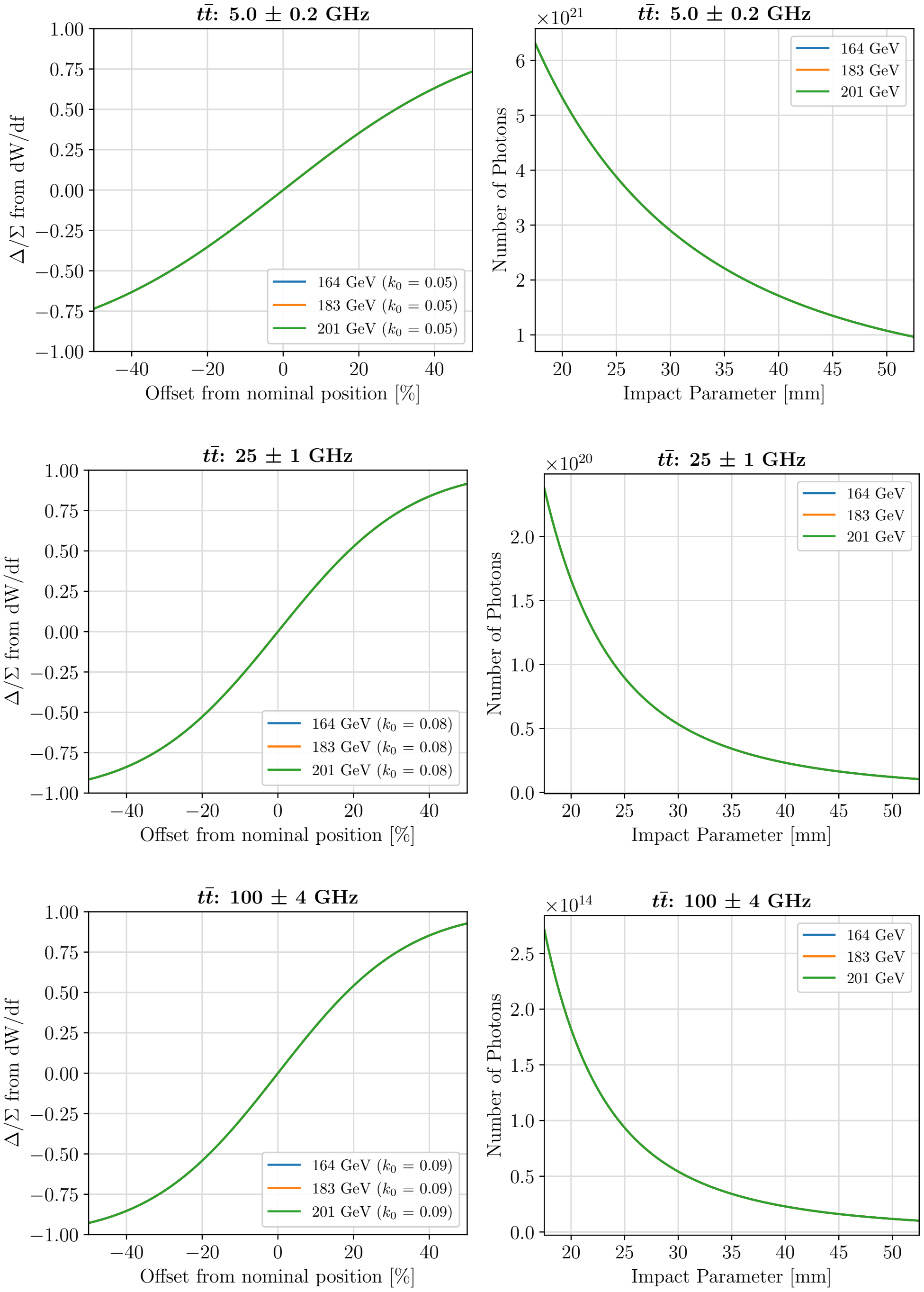

Figure A.8: Δ/Σ and number of photons for a 183 GeV electron/positron bunch. First row shows band pass filter centered at 5 GHz, second row at 25 GHz and third row at 100 GHz.

List of Figures

List of Tables

Symbols and Acronyms

$\boldsymbol{\vec{S}}$	Poynting vector
$\boldsymbol{F_{3D}}$	Bunch form factor
$\boldsymbol{N}$	Number of particles
$\boldsymbol{S_{3D}}$	Particle density distribution
$\boldsymbol{\beta}$	Velocity relative to the speed of light in vacuum ($= v/c$)
$\boldsymbol{\epsilon_0}$	Vacuum permittivity
$\boldsymbol{\epsilon_r}$	Relative permittivity
$\boldsymbol{\gamma}$	Lorentz factor
$\boldsymbol{\lambda}$	Wavelength
$\boldsymbol{\omega}$	Angular frequency
$\mathbf{H}$	Higgs boson
$\mathbf{SiO_2}$	Silicon dioxide (fused silica)
$\mathbf{W/W^{\pm}}$	W bosons
$\mathbf{Z/Z^0}$	Z boson
$\mathbf{t\bar{t}}$	Top quark and top antiquark
$\boldsymbol{\vartheta_{Ch}}$	Cherenkov angle
$\boldsymbol{c}$	Speed of light in vacuum
$\boldsymbol{e}$	Elementary charge
$\boldsymbol{f}$	Frequency
$\boldsymbol{h}$	Impact parameter
$\boldsymbol{n}$	Refractive index
$\boldsymbol{v}$	Velocity
BPM	Beam Position Monitor
CERN	European Organization for Nuclear Research
CESR	Cornell Electron Storage Ring
ChDR	Cherenkov diffraction radiation
ChR	Cherenkov radiation
CLEAR	CERN Linear Electron Accelerator for Research
FCC-ee	Future Circular Collider for electrons (e^-) and positrons (e^+)
LHC	Large Hadron Collider
PTFE	Teflon (Polytetrafluoroethylene)

Acknowledgements

I want to thank Professor Benedikt for introducing me into the fascinating world of accelerator physics and enabling me to perform my studies at the very centre of particle physics in Europe. Many thanks to Thibaut for his continuous support throughout all stages of this thesis. You have been such a wonderful supervisor during all this time, not just sharing your knowledge and expertise with me but even your office space. Many thanks also to Kacper for all the help and feedback you provided. It was a pleasure working with you, and I am looking forward to future collaborations. Also many thanks to the whole team working on Cherenkov diffraction radiation for all their feedback and fruitful discussion, especially Pavel, Stefano and Dan. Thanks a lot to Michele and Eugenio for introducing me to the experiments at CLEAR and always lending me a helping hand. Thanks to all the operators at CLEAR for providing their expertise and support. Furthermore, I want to thank the whole Intensity and Tune section for welcoming me during this time of social distancing. Also, thanks to the Beam Position section for sharing all the entertaining lunch breaks with us even at freezing temperatures.

Special thanks to my whole family. To my parents for supporting me in every way possible, no matter where I go. To my sisters and their own families for all their interest and encouragement. To the family of my wife for being family to me as well and their continuous support. Beyond that, I would like to thank Georg, Simon and especially Alex, for their unmatched company during our studies in Vienna and most of all their friendship.

Finally, I want to thank my wife Elisa for enriching my life every day no matter how many confinements we have to cope with.

Bibliography

[AAA+19] A. Abada, M. Abbrescia, S. Abdussalam, I. Abdyukhanov, J. Fernandez, A. Abramov, M. Aburaia, A. Acar, P. Adzic, P. Agrawal, O. Saavedra, J. Aguilera-Verdugo, M. Aiba, I. Aichinger, G. Aielli, A. Akay, A. Akhundov, H. Aksakal, J. Albacete, et al. FCC-ee: The lepton collider. *The European Physical Journal Special Topics*, 228:261–623, 06 2019.

[AFK18] K. Akai, K. Furukawa, and H. Koiso. SuperKEKB collider. *Nuclear Instruments and Methods in Physics Research Section A: Accelerators, Spectrometers, Detectors and Associated Equipment*, 907:188–199, Nov 2018.

[BAK+19] M. Bergamaschi, A. Aryshev, P. Karataev, R. Kieffer, T. Lefèvre, K. Lekomtsev, S. Mazzoni, A. Potylitsyn, and A. Schloegelhofer. Recent results using incoherent Cherenkov diffraction radiation for non-invasive beam diagnostics. In *10th International Particle Accelerator Conference*, page WEPGW077, 2019.

[CAH06] M. Collins and B. Al-Hashimi. On-chip time measurement architecture with femtosecond timing resolution. *Eleventh IEEE European Test Symposium (ETS'06)*, pages 103–110, 2006.

[Cas97] M. Castellano. A new non-intercepting beam size diagnostics using diffraction radiation from a slit. *Nuclear Instruments and Methods in Physics Research Section A: Accelerators, Spectrometers, Detectors and Associated Equipment*, 394(3):275 – 280, 1997.

[CBC+20] A. Curcio, M. Bergamaschi, R. Corsini, W. Farabolini, D. Gamba, L. Garolfi, R. Kieffer, T. Lefèvre, S. Mazzoni, K. Fedorov, J. Gardelle, A. Gilardi, P. Karataev, K. Lekomtsev, T. Pacey, Y. Saveliev, A. Potylitsyn, and E. Senes. Noninvasive bunch length measurements exploiting Cherenkov diffraction radiation. *Phys. Rev. Accel. Beams*, 23:022802, Feb 2020.

[Che37] P.A. Cherenkov. Visible radiation produced by electrons moving in a medium with velocities exceeding that of light. *Phys. Rev.*, 52:378–379, 1937.

[CHL$^+$17] J. Corbett, X. Huang, C. Li, T. Mitsuhashi, J. Wu, Y. Xu, and W. Zhang. Transverse Beam Profiling and Vertical Emittance Control with a Double-Slit Stellar Interferometer. In *5th International Beam Instrumentation Conference*, page MOPG70, 2017.

[Cus20] Cush. URL: `https://commons.wikimedia.org/wiki/File:Standard_Model_of_Elementary_Particles.svg`, Nov 2020.

[Dia19] Diamond-II conceptual design report. URL: `https://www.diamond.ac.uk/Home/About/Vision/Diamond-II.html`, May 2019. Oxfordshire, U.K.

[FBB$^+$19] Stefan Funkner, Edmund Blomley, Erik Bründermann, Michele Caselle, Nicole Hiller, Michael Nasse, Gudrun Niehues, Lorenzo Rota, Patrik Schönfeldt, Sophie Walther, Marc Weber, and Anke-Susanne Müller. High throughput data streaming of individual longitudinal electron bunch profiles. *Physical Review Accelerators and Beams*, 22, 02 2019.

[FT37] I.M. Frank and I.E. Tamm. Coherent visible radiation of fast electrons passing through matter. *Compt. Rend. Acad. Sci. URSS*, 14(3):109–114, 1937.

[G$^+$18] D. Gamba et al. The CLEAR user facility at CERN. *Nucl. Instrum. Meth. A*, 909:480–483, 2018.

[GDHR$^+$08] O. Grimm, H. Delsim-Hashemi, J. Rossbach, V. Balandin, and N. Golubeva. Transverse Electron Beam Size Effect on the Bunch Profile Determination with Coherent Radiation Diagnostics. *Conf. Proc. C*, 0806233:TUPC030, 2008.

[GS06] O. Grimm and P. Schmüser. Principles of longitudinal beam diagnostics with coherent radiation. *TESLA-FEL Report (2006),*, 01 2006.

[H$^+$20] D.M. Harryman et al. Properties of Cherenkov diffraction radiation as predicted by the polarisation currents approach for beam instrumentation, Sep 2020. Presented at International Beam Instrumentation Conference (IBIC 2020), held remotely, paper THPP05.

[JAB$^+$12] A. Jeff, M. Andersen, A. Boccardi, S. Bozyigit, E. Bravin, T. Lefèvre, A. Rabiller, F. Roncarolo, C. P. Welsch, and A. S. Fisher. Longitudinal density monitor for the lhc. *Phys. Rev. ST Accel. Beams*, 15:032803, Mar 2012.

[JMS$^+$19] R. Jones, N. Mounet, A. Schloegelhofer, D. Harryman, V.V. Bleko, S. Gogolev, J. Markova, D. Shkitov, M. Billing, J. Conway, Y. Fuentes, J. Shanks, J. Gardelle, M. Bergamaschi, R. Kieffer, T. Lefèvre, S. Mazzoni, F. Kirill, and A. Curcio. Cherenkov diffraction radiation as a tool for beam diagnostics. In *Proceedings, International Beam Instrumentation Conference (IBIC 2019): Malmö, Sweden*, 10 2019.

[KBB$^+$18] R. Kieffer, L. Bartnik, M. Bergamaschi, V. V. Bleko, M. Billing, L. Bobb, J. Conway, M. Forster, P. Karataev, A. S. Konkov, R. O. Jones, T. Lefèvre, J. S. Markova, S. Mazzoni, Y. Padilla Fuentes, A. P. Potylitsyn, J. Shanks, and S. Wang. Direct observation of incoherent Cherenkov diffraction radiation in the visible range. *Phys. Rev. Lett.*, 121:054802, Aug 2018.

[KG19] R. Kersevan and C. Garion. Design of the vacuum system of the FCC-ee electron-positron collider. In *10th International Particle Accelerator Conference*, page TUPMP035, 2019.

[KMP$^+$18] A.S. Konkov, J.S. Markova, A.P. Potylitsyn, V.V. Bleko, V.V. Soboleva, and P.V. Karataev. Theoretical model for incoherent Cherenkov diffraction radiation report ii. *Tomsk Polytechnic University Internal Report*, Apr 2018.

[KPJ07] R. Kitamura, L. Pilon, and M. Jonasz. Optical constants of silica glass from extreme ultraviolet to far infrared at near room temperature. *Appl. Opt.*, 46(33):8118–8133, Nov 2007.

[L$^+$18] T. Lefèvre et al. Non-invasive beam diagnostics with Cherenkov diffraction radiation. In *Proceedings, 9th International Particle Accelerator Conference (IPAC 2018): Vancouver, BC Canada, April 29-May 4, 2018*, page WEPAF074, 2018.

[L$^+$20] K. Łasocha et al. Simulation of Cherenkov diffraction radiation for various radiator designs, Sep 2020. Presented at International Beam Instrumentation Conference (IBIC 2020), held remotely, paper TUPP28.

[Lef19a] T. Lefèvre. Beam instrumentation for FCC-ee. URL: `https://indico.cern.ch/event/727555/contributions/`

`3452835/attachments/1870173/3077203/BI_FCCee_2019.pdf`, Jun 2019.

[Lef19b] T. Lefèvre. Cherenkov diffraction radiation as a tool for beam diagnostics. URL: `https://indico.cern.ch/event/842625/contributions/3536606/attachments/1904161/3144366/ChDR_IBIC2019.pdf`, Oct 2019.

[LS96] R. Lai and A. J. Sievers. Determination of bunch asymmetry from coherent radiation in the frequency domain. *AIP Conference Proceedings*, 367(1):312–326, 1996.

[Mou12] N. Mounet. *The LHC Transverse Coupled-Bunch Instability*. PhD thesis, École Polytechnique Fédérale de Lausanne, 2012.

[MOZ16] T. Mitsuhashi, K. Oide, and F. Zimmermann. Conceptual Design for SR Monitor in the FCC Beam Emittance (Size) Diagnostic. In *7th International Particle Accelerator Conference*, page MOPMB022, 2016.

[MTTS15] M. Masaki, S. Takano, M. Takao, and Y. Shimosaki. X-ray fresnel diffractometry for ultralow emittance diagnostics of next generation synchrotron light sources. *Phys. Rev. ST Accel. Beams*, 18:042802, Apr 2015.

[OK80] H. A. Olsen and H. Kolbenstvedt. Čerenkov radiation and transition radiation from small systems: Čerenkov radiation generated in a cylinder. *Phys. Rev. A*, 21:1987–1990, Jun 1980.

[PBB$^+$18] A. Papash, E. Blomley, M. Brosi, J. Gethmann, B. Kehrer, A. Müller, P. Schönfeldt, M. Schuh, and J. Steinmann. Non-linear optics and low alpha operation at the storage ring kara at kit. In *9th International Particle Accelerator Conference*, 05 2018.

[Pol20] Mikhail N. Polyanskiy. Refractive index database. URL: `https://refractiveindex.info`, Oct 2020.

[S$^+$18] Johannes L. Steinmann et al. Continuous bunch-by-bunch spectroscopic investigation of the microbunching instability. *Phys. Rev. Accel. Beams*, 21(11):110705, 2018.

[SAL$^+$19] K. Sjøbæk, E. Adli, C. Lindstrøm, M. Bergamaschi, S. Burger, R. Corsini, A. Curcio, S. Curt, S. Doebert, W. Farabolini, D. Gamba,

L. Garolfi, A. Gilardi, I. Gorgisyan, E. Granados, H. Guerin, R. Kieffer, M. Krupa, T. Lefèvre, and A. Lyapin. Status of the clear electron beam user facility at cern. In *Proceedings, 10th International Particle Accelerator Conference (IPAC 2019): Melbourne, Australia*, 07 2019.

[Sha20] Dmitry Shatilov. personal communication, Apr 2020. (CERN, BE-ABP-HSS).

[SK14] M. Shevelev and A. Konkov. Peculiarities of the generation of Vavilov-Cherenkov radiation induced by a charged particle moving past a dielectric target. *Journal of Experimental and Theoretical Physics*, 118:501, 04 2014.

[SPP$^+$17] M. Siano, B. Paroli, M.A.C. Potenza, U. Iriso, A.A. Nosych, L. Torino, S. Mazzoni, G. Trad, and A.N. Goldblatt. Characterizing temporal coherence of visible synchrotron radiation with heterodyne near field speckles. *Phys. Rev. Accel. Beams*, 20(11):110702, 2017.

[Tam39] I.E. Tamm. Radiation emitted by uniformly moving electrons. *Journal of Physics (USSR)*, 1:439–454, 1939.

[TdF60] G. Toraldo di Francia. On the theory of some Čerenkovian effects. *Il Nuovo Cimento (1955-1965)*, 16:61–77, 1960.

[Ulr66] R. Ulrich. Zur Cerenkov-Strahlung von Elektronen dicht über einem Dielektrikum. *Zeitschrift für Physik*, 194, Apr 1966.

[WBB$^+$06] C. Welsch, H. Braun, E. Bravin, R. Corsini, S. Doebert, T. Lefèvre, F. Tecker, P. Urschütz, B. Buonomo, O. Coiro, A. Ghigo, and B. Preger. Longitudinal beam profile measurements at ctf3 using a streak camera. *Journal of Instrumentation*, 1:P09002, 09 2006.